

1 **Magneto-acoustic protein nanostructures for non-invasive imaging of tissue**
2 **mechanics *in vivo***

3
4 Whee-Soo Kim^{1,2,3,#}, Sungjin Min^{4,#}, Su Kyeom Kim⁴, Sunghwi Kang^{2,3}, Hunter Davis¹,
5 Avinoam Bar-Zion¹, Dina Malounda¹, Yu Heun Kim⁴, Soohwan An⁴, Jae-Hyun Lee^{2,3}, Soo Han
6 Bae^{5,6}, Jin Gu Lee⁷, Minsuk Kwak^{2,3}, Seung-Woo Cho^{2,3,4,†}, Mikhail G. Shapiro^{1,2,3,†}, Jinwoo
7 Cheon^{2,3,†},

8 ¹Division of Chemistry and Chemical Engineering, California Institute of Technology, Pasadena,
9 CA 91125, USA

10 ²Center for Nanomedicine, Institute for Basic Science (IBS), Seoul 03722, Republic of Korea

11 ³Graduate Program of Nano Biomedical Engineering (NanoBME), Advanced Science Institute,
12 Yonsei University, Seoul 03722, Republic of Korea

13 ⁴Department of Biotechnology, Yonsei University, Seoul 03722, Republic of Korea

14 ⁵Severance Biomedical Science Institute, Yonsei Biomedical Research Institute, Yonsei
15 University College of Medicine, Seoul 03722, Republic of Korea

16 ⁶Severance Biomedical Science Institute, Graduate School of Medical Science, Brain Korea 21
17 Project, Yonsei University College of Medicine, Seoul 03722, Republic of Korea

18 ⁷Department of Thoracic and Cardiovascular Surgery, Severance Hospital, Yonsei University
19 College of Medicine, Seoul 03722, Republic of Korea

20 # W.S. Kim and S. Min equally contributed.

21 † To whom correspondence should be addressed:

22 jcheon@yonsei.ac.kr, mikhail@caltech.edu, or seungwoocho@yonsei.ac.kr

23

24

25 **Abstract**

26 Measuring cellular and tissue mechanics inside intact living organisms is essential for
27 interrogating the roles of force in physiological and disease processes, and is a major goal in the
28 field of mechanobiology. However, existing biosensors for 3D tissue mechanics, primarily based
29 on fluorescent emissions and deformable materials, are limited for *in vivo* measurement due to
30 the limited light penetration and poor material stability inside intact, living organisms. While
31 magneto-motive ultrasound (MMUS), which uses superparamagnetic nanoparticles as imaging
32 contrast agents, has emerged as a promising modality for real-time *in vivo* imaging of tissue
33 mechanics, it has poor sensitivity and spatiotemporal resolution. To overcome these limitations,
34 we introduce magneto-gas vesicles (MGVs), a unique class of protein nanostructures based on
35 gas vesicles and magnetic nanoparticles that produces differential ultrasound signals in response
36 to varying mechanical properties of surrounding tissues. These hybrid protein nanostructures
37 significantly improve signal strength and detection sensitivity. Furthermore, MGVs enable non-
38 invasive, long-term, and quantitative measurement of mechanical properties within 3D tissues
39 and organs *in vivo*. We demonstrated the performance of MGV-based mechano-sensors *in vitro*,
40 in fibrosis models of organoids, and *in vivo* in mouse liver fibrosis models.

41

42

43

44

45

46 **Introduction**

47 Tissue mechanical properties are critical regulators of cellular processes driving
48 morphogenesis, tissue homeostasis, and disease progression¹. Particularly, tissue stiffness is
49 significantly altered during many pathological processes including cancer, diabetes,
50 cardiovascular disease, and fibrosis². The ability to measure the localized tissue stiffness within
51 3D living, deep tissues is vital to understanding organismal development and disease processes³.
52 However, measuring cellular-scale and multi-directional forces within living, three-dimensional
53 tissues remains challenging⁴. A large repertoire of techniques has been developed to measure
54 mechanics at subcellular resolution, but they are limited to *in vitro* measurement of near-surface
55 stiffness in 2D cultured cells or dissected tissues⁵⁻⁸. Moreover, measurements at this length scale
56 are different from tissue-level mechanical properties. Macroscopic characterization methods such
57 as traction force microscopy, rheometry, and elastic micropillars have been used to measure
58 forces at supracellular length scale⁹⁻¹¹.

59 However, these approaches cannot capture local variations in tissue stiffness, and have
60 only been performed in 2D/3D cell cultures and dissected tissue sections. Shear-wave
61 elastography represents an ultrasound-based method for non-invasive and quantitative
62 assessment of *in vivo* tissue stiffness, but it may have limited resolution making it difficult to
63 detect small tumors, boundary difficulties, and wave speed fluctuation in different tissue types¹².
64 Recently, several strategies based on injectable and deformable materials such as micrometre-
65 sized oil droplets or hydrogels have enabled quantitative measurement of local mechanical
66 properties within intact soft tissues *in vivo*^{4,13-15}. However, these methods rely on fluorescent
67 probes and optical imaging, and thus deploying such biosensors inside deep tissue of living
68 organisms is challenging due to the limited penetration of light in tissue¹⁶. Furthermore, these

69 materials may be sensitive to local factors, such as pH and temperature, limiting the capability of
70 long-term, *in vivo* measurement of tissue mechanics¹⁷.

71 Magnetomotive ultrasound imaging (MMUS) has emerged as a promising ultrasound-
72 based technique capable of measuring mechanical properties of intact tissues *in vivo*¹⁸. In this
73 method, an external magnetic field induces movement of magnetic nanoparticles (MNPs) and
74 consequently displacement of surrounding tissues, which can be detected by ultrasound imaging,
75 permitting a qualitative inference of mechanical properties of the tissues^{19,20}. However, MNPs
76 are sub-optimal contrast agents for ultrasound detection because they have much lower acoustic
77 scattering compared to typical gas-filled ultrasound contrast agents. As a result, MMUS has poor
78 signal-to-noise ratio and low spatial resolution, and requires a high dose of MNPs and bulky
79 magnetic set-up, both of which present challenges in quantification of tissue mechanics *in vivo*¹⁸.

80 Gas vesicles are a unique class of air-filled protein nanostructures purified from buoyant
81 photosynthetic microorganisms which act as highly sensitive ultrasound contrast agents for non-
82 invasive imaging due to their unique physical properties and scattering of sound waves^{16,21,22}. In
83 this study, we developed magneto-GVs (MGVs) – nanoengineered conjugates of GVs and
84 strongly superparamagnetic nanoparticles. MGVs produce strong MMUS contrast, allowing the
85 direct measurement of local mechanical properties in 3D organoids and living, intact tissues
86 while overcoming the limitations of the current MMUS imaging technique. Based on the
87 principle of MMUS imaging, we hypothesized that we could develop GV-based *in vivo* tissue
88 mechano-sensors that dynamically change their ultrasound contrast in response to differential
89 tissue mechanics. As the mobility of nanoparticles is influenced by the mechanical properties of
90 their surroundings, an increase in surrounding tissue stiffness reduces magnetically induced
91 movement of MGVs and hence decreases MMUS signals. At the same time, the intrinsic ability

92 of GVs to produce nonlinear ultrasound contrast distinct from MMUS provides a measure of
93 MGV concentration in tissues. Therefore, MGV-based MMUS imaging can quantitatively
94 measure various levels of tissue stiffness *in vivo* with enhanced detection limits, sensitivity
95 compared to conventional MMUS contrast agents such as MNPs. With excellent material
96 stability under physiological conditions, MGVs allow for robust and reproducible imaging that is
97 demonstrated in a single application, greatly advancing the *in vivo* capability of MMUS for long-
98 term biological imaging such as monitoring disease progression. In this study, we demonstrated
99 the utility of MGVs for sensitive and quantitative measurement of tissue stiffness through *in vitro*
100 and *in vivo* experiments. We also demonstrated that the unique properties of MGVs could enable
101 long-term disease monitoring and drug screening using *in vitro* 3D organoid and *in vivo* fibrosis
102 models.

103

104 **Results**

105 **Development of MGVs and characterization with MMUS imaging**

106 To determine whether the combination of particles with high acoustic contrast and strong
107 superparamagnetism can improve the MMUS imaging capability, we synthesized magnetic
108 nanoparticle-conjugated gas vesicles (MGVs). We established the MMUS imaging system and
109 optimized the system's magnetic properties using standard magnetic microparticles (**Fig. 1a**,
110 **Supplementary Fig. 1**). Based on the MMUS signal intensity, magnetic parameters of 5 Hz, 30
111 mT, and sine wave were chosen as frequency, max field strength, and temporal pattern of the
112 electromagnetic field, respectively (**Supplementary Fig. 1**). Zinc-doped iron oxide magnetic
113 nanoparticles (MNPs) were synthesized and functionalized with azide groups, as previously
114 reported²³. We purified GVs from the cyanobacterium *Anabaena flos-aquae*²⁴, and added
115 dibenzocyclooctyne (DBCO) to the GV protein surface through an NH₂-NHS reaction. MGVs
116 were finally synthesized by conjugating azide-functionalized MNPs and DBCO-GVs via click
117 chemistry (**Fig. 1b**). After a 4-hr conjugation reaction, MGVs could be isolated from a
118 suspension of unbound MNPs using buoyancy purification (**Fig. 1d**). MGVs had a hydrodynamic
119 diameter of approximately 494.1±11.5 nm, while functionalized GVs had a diameter of
120 approximately 272±4.5 nm (**Fig. 1c**). MGVs were stable in different media conditions or during
121 prolonged storage (**Supplementary Fig. 2a-b**). The conjugation ratio of MNPs to GVs was
122 approximately 186 MNPs per GV (**Fig. 1e**, **Supplementary Fig. 3**). The magnetic moment of
123 MGVs was 79 emu/g, which was comparable to that of MNPs (**Fig. 1f**).

124 We next assessed the ability of MGV protein nanostructures to produce robust MMUS signals in
125 response to applied magnetic fields. Using the optimized magnetic conditions identified above,
126 we performed a head-to-head comparison of GVs, MNPs, and MGVs with MMUS imaging in

127 agarose phantoms. The concentrations of all materials were matched based on ICP
128 measurements and B-mode imaging (**Fig. 1g, Supplementary Fig. 3**). MGVs clearly
129 outperformed other nanomaterials in terms of sensitivity and spatiotemporal control, while the
130 spatial resolution of MMUS imaging largely retained the resolution of conventional B mode
131 ultrasound (**Supplementary Fig. 4**). Magnetic stimulation of MGVs resulted in robust
132 ultrasound signals, whereas turning off the magnetic field eliminated scattering signals. While
133 both GVs and MGVs produced similar ultrasound contrast using a conventional B-mode
134 sequence, MGVs achieved a 12-fold higher magnetic field-dependent signal intensity change (Δ ,
135 110.1 ± 21.3) than GVs (9.1 ± 8.7) (**Fig. 1g-j**). In addition, MGVs produced a significant increase
136 in the delta contrast signal compared to MNPs of Fe_2O_3 (25.6 ± 16.6) and Al_2O_3 (26.5 ± 14.9),
137 suggesting the ability of GVs conjugated to zinc-doped iron oxide MNPs to transduce magnetic
138 stimulation, strongly scatter sound waves, and produce ultrasound contrast for greatly improved
139 MMUS sensitivity (**Fig. 1g-j**).

140 To evaluate the performance limits of MGV-based MMUS imaging, we first performed imaging
141 of a dispersion containing MGVs, GVs, and MNPs at a fixed concentration of 0.4 nM in 0.1%
142 agarose while applying magnetic fields with increasing strength ranging from 7 mT to 30 mT. A
143 decrease in magnetic strength was achieved by moving the sample further away from the magnet.
144 MMUS imaging of MGVs revealed a robust non-linear magnetic MMUS response, but not in the
145 negative control of GVs, which produced no visible contrast in response to any level of magnetic
146 field. The MGVs showed a gradual increase of MMUS signal with detectable signals appearing
147 at 10 mT and continuing to increase until 30 mT. In contrast, MNPs produced detectable but
148 substantially weaker MMUS signal only when exposed to a magnetic field ≥ 30 mT (**Fig. 1h-k**).
149 To assess the sensitivity of the MGV-based approach relative to other nanomaterials, we

150 performed MMUS imaging of a concentration series of MGVs, GVs, and MNPs in agarose
151 phantoms with a constant 30 mT magnetic field. MGVs produced significantly higher delta
152 contrast signals than the other control materials when the concentration was in the range of 0.05
153 to 0.4 nM (**Fig. 1i-l**). MGVs attained excellent signal-to-background ratio with a limit of
154 detection (LOD) of 0.05 nM, representing over 8-fold enhancement in sensitivity relative to
155 conventional MNP-based MMUS imaging (**Fig. 1i-l**). When we compared our results with
156 MGVs to previously published MNP-based MMUS imaging results, we found that MGV-based
157 MMUS uniquely combined sensitivity to relatively low MNP concentrations and relatively weak
158 magnetic fields (**Supplementary Fig. 5**). Altogether, these results suggest that conjugating GVs
159 with MNPs into a hybrid magnetoacoustic material results in novel contrast agents for MMUS
160 imaging with enhanced ultrasound contrast and detection sensitivity.

161

162 **Validation of MGV system in different stiffness conditions**

163 The material stiffness influences the magnetically induced motion of magnetic nanoparticles¹⁹.
164 Whereas softer materials would allow more MGV movement and induce stronger ultrasound
165 scattering, stiffer materials would restrict MGV motion in response to applied magnetic fields,
166 leading to a decrease in MMUS signal (**Fig. 2a**). To test the ability of MGVs to quantitatively
167 measure the stiffness of surrounding materials, we performed MMUS imaging *in vitro* of MGVs
168 embedded in agarose phantoms with varying elastic modulus, ranging from 74 Pa to 5828 Pa
169 (**Fig. 2b**). As predicted, we observed an inverse relationship of MGV signals as a function of
170 increasing elastic modulus of the agarose phantoms. At fixed MGV concentrations ($OD_{500} = 4$,
171 0.4 nM) and magnetic field (30 mT), MGVs in 0.1% agarose (109.1 ± 52.3) produced a 2- and 6-
172 fold greater MMUS signal intensity change than in 0.15% agarose (56.9 ± 38.8) and 0.2% agarose

173 (18.7±15.3), respectively, while generating negligible signal in 0.5% agarose phantom (9.3±3.1)
174 (**Fig. 2b-c**). While the MNP-only sample showed stiffness-dependent signal intensity changes, its
175 MMUS signal was significantly weaker than that of MGVs, leading to lower detection sensitivity
176 of material stiffness (**Fig. 2b-c**). These results together demonstrate that MGVs embedded in
177 phantoms with lower elastic moduli experience more strain from the same applied magnetic
178 gradient force, resulting in larger vibration amplitudes and stronger ultrasound signals.

179 To determine whether MGVs can more precisely quantify a wide range of material stiffness
180 values, we used two *in vitro* phantoms created from two different hydrogel systems with varying
181 stiffness (**Fig. 2d, Supplementary Fig. 6**). Matrigel-based phantoms were used for softer
182 materials (63 Pa), and agarose gel phantoms were used for materials with elastic moduli ranging
183 from 74 to 5828 Pa. We observed that the detection range varies with MGV concentration (**Fig.**
184 **2d-e**). The MMUS signal was clearly differentiated in a range of around 63 Pa (100.2±31.7) to
185 564 Pa (10.0±6.9) when using 0.2 nM MGVs, whereas the detection range broadened to 5,828 Pa
186 (24.3±4.9) when using 0.8 nM MGVs (**Fig. 2d-e**). Furthermore, when very small amounts of
187 MGVs (0.05 nM) were used, the MMUS signal was only visible until 74 Pa, indicating that at
188 this concentration, MGVs are capable of detecting stiffness changes in materials with elastic
189 moduli less than 74 Pa (**Fig. 2d-e**). These findings show that depending on the tissue being
190 measured, MGV concentration can be adjusted to generate enhanced or attenuated signals for the
191 acquisition of more accurate MMUS images in diverse tissue types. Moreover, these results
192 demonstrate that MGVs can be utilized as a stiffness sensor, as their signals are connected to the
193 rigidity of their surroundings. In other words, the tissue visualization may vary based on the
194 MGV concentration employed. It would also be feasible to evaluate how the tissue mechanics
195 change over time using the same MGV concentration. To demonstrate this concept, we

196 constructed an organoid model with increasing stiffness in response to the progression of fibrosis.

197 **Validation of MGV system using lung organoid fibrosis model**

198 Organoids are miniaturized organ-like constructs, and they are in the spotlight as a novel *in vitro*
199 platform to study the development and modeling of disease because they can implement the
200 developmental processes and functional characteristics of actual organs²⁵. To confirm the
201 applicability of MGVs in monitoring the tissue- and cellular-level stiffness of 3D
202 microenvironments, a lung fibrosis model was developed with lung organoids. Because lung
203 fibrosis causes tissue stiffening, which leads to a decline in respiratory function and subsequently
204 increased mortality²⁶, it is critical to diagnose lung fibrosis at an early stage. Fibrosis was
205 induced by culturing lung organoids with transforming growth factor (TGF)- β to activate TGF- β
206 signaling²⁷⁻²⁹. While normal lung organoids continued to grow in size, fibrotic lung organoids
207 started to decrease in size from day 5 of TGF- β induced fibrosis. Also, we observed that the
208 higher the concentration of TGF- β , the smaller the fibrotic lung organoids became, indicating
209 that the severity of fibrosis was dependent on the level of TGF- β signal activation
210 **(Supplementary Fig. 7).**

211 To demonstrate the capability of MGV-based MMUS imaging for sensitive detection of fibrosis
212 progression in a lung organoid model, MGVs were microinjected into the lumen of lung
213 organoids using a Pasteur pipette, and the difference in MMUS signals was compared between
214 normal and fibrosis organoids **(Fig. 3a)**. Microinjection of MGVs conjugated with fluorescence
215 markers showed that MGVs filled the lumen of lung organoids and remained there for 19 days
216 without leakage **(Fig. 3b, Supplementary Fig. 8)**. Consistent with *in vitro* experiments, MGVs
217 produced significantly enhanced MMUS signals compared to GVs and MNPs in the lumen of
218 lung organoids **(Fig. 3c)**. We hypothesized that fibrotic organoids would exhibit an increased

219 stiffness, which would suppress the magnetically induced movements of MGVs and thus result
220 in weaker MMUS signals (**Fig. 3d**). Lung organoids were moved to a polydimethylsiloxane
221 (PDMS) mold 2 days after MGV microinjection, and the next day fibrosis in MGV-injected
222 organoids was induced with TGF- β treatment using a range of concentrations. MMUS imaging
223 was performed from day 5 to 16 after the induction of fibrosis. The intensity of MMUS signals
224 gradually decreased in the fibrotic lung organoids over a culture period of 5 to 16 days,
225 indicating that lung stiffness increased during the fibrosis progression, and the decrease in signal
226 was more evident in the organoids treated with 50 ng/mL TGF- β (**Fig. 3e-f**). Our results
227 demonstrate that MMUS imaging using MGVs could provide significant advantages in the
228 detection of fibrosis over other techniques by allowing real-time monitoring of stiffness changes
229 in live lung organoids without fixation.

230 To validate the increased fibrosis-induced stiffness in lung organoids observed by MMUS, we
231 performed histological and immunohistochemical analyses. Hematoxylin & eosin (H&E)
232 staining revealed thickening of the epithelium layer, abnormal cell growth, and MGV
233 localization in the lumen of TGF- β -treated lung organoids in a dose-dependent manner (**Fig. 3g**).
234 Moreover, the expression of the known markers that identify ciliated cells (α -tubulin) and goblet
235 cells (MUC5AC) was markedly reduced, while the increased presence of P63-positive basal cells
236 was observed in fibrotic lung organoids with TGF- β treatment (**Supplementary Fig. 9**).
237 Furthermore, we found a significantly increased expression of smooth muscle actin (SMA) and
238 vimentin (VIM), markers of the epithelial-to-mesenchymal transition (EMT), in basal cells in
239 fibrotic organoids (**Supplementary Fig. 9**). Previous studies showed that in the airway
240 epithelium in patients with idiopathic pulmonary fibrosis (IPF), ciliated cells and goblet cells
241 decrease in number while basal cells proliferate, and the occurrence of EMT in these basal cells

242 results in the formation of fibroblastic foci³⁰. These pathological events that form fibroblastic
243 foci in the lumen could lead to increased stiffness in lung organoids. Finally, we examined the
244 feasibility of the MGV-bearing lung organoid model for evaluating the efficacy of anti-fibrosis
245 drugs (**Fig. 3h**). Nintedanib, well-known for its anti-fibrotic and anti-inflammatory effects on IPF,
246 was tested, and drug treatment was performed starting from the 5th day after fibrosis induction³¹.
247 We found that the intensity of MMUS signals decreased in organoids with TGF- β -induced
248 fibrosis, but the signals in lung fibrosis organoids treated with nintedanib did not decrease and
249 were maintained at a similar level to that of normal organoids (**Fig. 3h-i**). Based on this result,
250 we verified that MGV imaging in a lung organoid model could be used to screen therapeutic
251 drugs for lung fibrosis.

252 **MGV- based MMUS imaging in liver organoid fibrosis model**

253 The liver is another important organ for fibrosis modeling due to the high occurrence of hepatic
254 steatosis and cirrhosis. Tissue stiffness is known as an important indicator of the occurrence and
255 progression of fibrotic liver disease³². Accordingly, we tested MGV-based MMUS imaging for
256 detecting the increase in stiffness in a liver fibrosis organoid model. As liver organoids do not
257 have a cavity into which MGVs could be injected, an alternative method of MGV incorporation
258 into organoids was considered. Four types of cells (hepatic endodermal cells, hepatic stellate
259 cells, endothelial cells, and mesenchymal cells) were encapsulated in collagen hydrogel
260 containing MGVs, resulting in generation of MGV-incorporated liver organoids (**Fig. 4a**). Then,
261 fibrosis was induced by TGF- β treatment. Direct encapsulation of MGVs during organoid
262 development allowed localization of MGVs in the extracellular matrix (ECM) in organoids,
263 where the increase in stiffness actually occurs³³. Because hepatic stellate cells are an important
264 cell type in liver fibrosis and collagen is an ECM component highly correlated with increased

265 stiffness in liver fibrosis, our liver organoid platform contains both cellular and extracellular
266 components suitable for modeling fibrosis. We confirmed the localization of hepatic endodermal
267 cells and hepatic stellate cells in the MGV-incorporated liver organoids, which mimics the
268 cellular compositions of liver tissue (**Fig. 4b**). Hence, we hypothesized that our liver organoids
269 create a more physiologically accurate model and that MGVs can more accurately sense the
270 increase in stiffness caused by liver fibrosis.

271 Induction of fibrosis in liver organoids was done in the same manner as in the lung organoids,
272 and MMUS imaging was performed from 0 to 7 days after induction (**Fig. 4c**). Although normal
273 and fibrosis liver organoids did not show morphological differences, there was a significant
274 difference between them in the intensity of the MMUS signals over the culture period (**Fig. 4d-e**).
275 This result shows that MGVs enable detection of changes in the stiffness of liver tissue.
276 Interestingly, the intensity of the MMUS signal gradually increased in normal liver organoids
277 during culture up to 7 days, indicating that the stiffness of liver organoids naturally decreased
278 over time, which may be attributed to active ECM remodeling during the development of liver
279 organoids³⁴⁻³⁶. In normal tissue, ECM homeostasis is regulated by repeated cycles of ECM
280 degradation and synthesis^{34,37}. To verify active ECM remodeling in developing organoids, we
281 checked the expression level of a major collagen component (collagen type I) in liver organoids
282 on days 7 and 10 in organoid culture (**Supplementary Fig. 10a-b**). Collagen type I content was
283 reduced in 10-day organoids when compared with 7-day organoids. Moreover, considerable
284 expression of matrix metalloproteinase 2 (MMP2) which degrades collagen type I was detected
285 in liver organoids (**Supplementary Fig. 10c**)³⁸. Thus, continuous degradation of collagen in liver
286 organoids by MMP2 enzymes secreted from activated cells during development may decrease
287 the stiffness of liver organoids and increase the MMUS intensity in normal liver organoids over

288 the culture period. The presence of MGVs in each organoid model was affirmed through H&E
289 staining of organoid sections (**Fig. 4f**). The induction of fibrosis was verified through the
290 upregulation of a fibrotic marker (VIM) and the reduction of a mature hepatic marker (albumin,
291 ALB) in liver organoids treated with TGF- β (**Fig. 4g**). Finally, we examined the applicability of
292 MGV-incorporated liver organoid models to test drugs to treat liver fibrosis. The intensity of
293 MMUS signals in fibrotic liver organoids treated with obeticholic acid, a drug known to prevent
294 or retard liver fibrosis and cirrhosis, was significantly higher than that of the fibrotic organoids
295 without drug treatment (**Fig. 4h-i**), indicating a significant reduction in stiffness and alleviation
296 of fibrosis by treatment with obeticholic acid. These data demonstrate the possibility of using
297 MGV-incorporated liver organoids as a drug screening platform for liver fibrosis. The
298 combination of MGV-based MMUS imaging and organoid technology could also be utilized for
299 other diseases in which a change in stiffness is an important diagnostic indicator, such as acidosis
300 of the brain and various types of cancers^{37,38}.

301 **MGVs signal detection in animal liver tissues**

302 Having demonstrated the ability of MGVs to serve as MMUS contrast agents and stiffness
303 sensors *in vitro* and *in cellulo*, we next tested their ability to produce robust MMUS signals and
304 measure the stiffness of animal tissues *ex vivo* and *in vivo*. To compare the performance of
305 MGVs, GVs, and MNPs as MMUS contrast agents *in vivo*, we performed intravenous injections
306 of these materials into live, anaesthetized mice. To facilitate more specific GV imaging contrast
307 against tissue background, we modified the protein composition of Ana GVs to generate
308 enhanced non-linear ultrasound contrast under amplitude modulation (AM) pulse sequences³⁹.
309 After 5 minutes post-injection, the liver was removed for *ex vivo* MMUS imaging (**Fig. 5a**). The
310 liver was chosen as our model organ because imaging stiffness would be useful for detecting

311 liver diseases. In addition, GVs naturally accumulate in the liver upon intravenous
312 administration^{40,41}. We expected intravenously administered MGVs to be rapidly taken up by the
313 liver, resulting in strong ultrasound contrast in the organ. We observed clear, robust MMUS
314 contrast by MGVs, which exhibited 10-fold stronger signals than those produced by GVs and
315 MNPs (**Fig. 5b-c**). To demonstrate that MGVs are capable of measuring the mechanical
316 properties of tissues *ex vivo*, MMUS imaging was done in liver samples fixed with 10% formalin
317 for 48 hours⁴². After formalin fixation, the MMUS signals from injected MGVs significantly
318 decreased, corresponding to an increase in tissue stiffness (**Fig. 5b-c**). Meanwhile, non-
319 magnetomotive AM ultrasound images produced comparable ultrasound contrast from MGVs
320 both before and after formalin fixation, indicating that the decrease in MMUS signal was not due
321 to the collapse or removal of MGVs during fixation, but rather likely due to a restriction of
322 magnetically induced MGV movement (**Supplementary Fig. 11**). Thus, *ex vivo* liver imaging
323 demonstrated that increasing stiffness lowered the MMUS signal, similarly as in the organoid
324 model.

325 Due to ultrasound reflection by the skin and breathing artifacts, which create significant noise
326 and signal attenuation, *in vivo* MMUS imaging of live animals remains challenging. B-mode and
327 Doppler imaging were used to locate the liver, and using ultrafast amplitude modulation (uAM)
328 imaging, we could visualize robust contrast from MGVs and GVs, confirming their delivery to
329 and accumulation in the liver (**Fig. 5e, Supplementary Fig. 12**). After confirming their
330 localization, we set out to test the ability of MGVs to produce robust ultrasound signals that can
331 be visualized in deep tissues by MMUS imaging to image an *in vivo* biological process within
332 live, breathing animals (**Fig. 5d**). This is an important challenge in non-invasive, deep tissue
333 imaging of tissue mechanics as it is well-documented that motion artifacts of live animals reduce

334 accuracy and sensitivity⁴³. We administered 100 μ L MGVs at 2.28 nM into the tail veins of mice,
335 and 5 min later performed MMUS imaging to image their delivery into the liver while animals
336 were being anesthetized. Both GVs and MGVs could be detected with enhanced signals in AM
337 images, while MNPs did not produce any detectable signals *in vivo*. We found that the mean
338 MMUS signal of MGVs (37.1 ± 6.5) was 9.3 \times and 6.4 \times stronger than that of GVs (4.0 ± 2.4) and
339 MNPs (5.8 ± 2.6), respectively (**Fig. 5e-f**). These results demonstrate that MGVs can be used as
340 MMUS contrast agents to improve signal strength and imaging sensitivity in more complex *in*
341 *vivo* models.

342 **Detection of liver fibrosis using MGVs**

343 After establishing MGVs as excellent contrast agents for *in vivo* MMUS imaging, we then asked
344 whether our MGV-based system can function as a stiffness sensor to diagnose *in vivo* disease
345 models. We injected C57BL/6 mice with carbon tetrachloride (CCl₄), a well-established
346 molecule to promote TGF- β signaling and collagen deposition, and induce liver fibrosis⁴⁴. By
347 administering CCl₄, hepatic stiffness increases concurrently with fibrosis induction, and the
348 stiffness increases until 30 days after injection and then plateaus⁴⁵. After 4 weeks of CCl₄
349 treatment, MMUS imaging was performed to assess the mechanical properties of fibrotic and
350 normal livers (**Fig. 6a**). Intravenously administered MGVs were taken up by liver tissues and
351 retained their ultrasound scattering property, as evidenced by robust ultrasound contrast under
352 AM. While AM imaging confirmed that similar quantities of MGVs were delivered to the livers
353 of both control and fibrotic mice, we observed a significant reduction in MMUS signal in the
354 fibrosis-induced cohort (**Fig. 6b**). A softness index, which we used as a quantitative indicator of
355 *in vivo* tissue stiffness based on MMUS and AM imaging, was significantly lower in the fibrosis
356 group (4.2 ± 1.0) than in normal controls (14.0 ± 4.6) (**Fig. 6c**), consistent with previous

357 observations that liver stiffness increases with the progression of fibrosis⁴⁵. Histological and
358 biochemical analyses confirmed the induction of liver fibrosis, as evidenced by pronounced
359 morphological alteration, disruption of tissue architecture, fiber extension, and increased
360 collagen accumulation (**Fig. 6d-f, Supplementary Fig. 13**). No signs of fibrosis or inflammation
361 were observed in control animals injected with MGVs only, suggesting excellent
362 biocompatibility of MGVs (**Fig. 6d-f**). Our results establish the ability of our magneto-acoustic
363 nanostructures to visualize and quantitatively detect tissue stiffness within the context of *in vivo*
364 imaging. This demonstration suggests that MGVs are useful as contrast agents for the non-
365 invasive, *in vivo* detection of diseases defined by mechanical changes, such as fibrosis and
366 cancer.

367

368 **Discussion**

369 Our results establish a new class of hybrid protein nanostructure (MGVs) as
370 nanomaterial-based magneto-acoustically modulated MMUS contrast agents for non-invasive
371 and sensitive imaging and measurement of tissue elasticity *in vivo*. The MGV-based imaging
372 modality couples the improved ultrasound imaging sensitivity of gas vesicles with the capacity
373 of MNPs enabling non-invasive, long-term, safe *in vivo* imaging to deepen our understanding of
374 whole tissue mechanics, compared to prior MMUS imaging or fluorescence-based mechano-
375 sensors^{4,18}. The ability of our MGVs to visualize and measure stiffness in 3D tissues *in vivo* was
376 demonstrated by successful detection and monitoring of fibrosis development and therapeutic
377 effects in 3D organoid and *in vivo* models.

378 Due to rapid uptake and accumulation of nanostructures by the liver, the clinical

379 potential of MGVs for accurate and non-invasive *in vivo* detection of hepatic fibrosis could be
380 readily tested for detecting hepatic fibrosis at an early stage and determining the efficacy of new
381 anti-fibrosis therapies. While a number of non-invasive techniques, such as magnetic resonance
382 imaging (MRI) and shear-wave elastography, have been employed to detect fibrosis, these
383 techniques are also limited by motion artifacts, sampling variability, and insufficient
384 sensitivity^{46,47}. Our findings establish magneto-gas vesicles as a promising new class of
385 biosensors for sensitive and non-invasive fibrosis detection *in vivo*. As the elastic modulus of
386 tissues are a reliable biophysical parameter for disease diagnosis⁴⁸, further application-centric
387 optimizations and development of imaging acquisition and processing will help MGV-based
388 imaging achieve widespread use. Additionally, because GV can be genetically encoded inside the
389 cells⁴⁹, combining GV expression with the formation of magnetic cellular nanomaterials, such as
390 magnetotactic bacteria⁵⁰, can home to specific tissues and sense molecular signals in their
391 environment in addition to tissue mechanics. With these improvements, we envision broad utility
392 of our protein nanosturcture as a powerful mechanobiology research platform for quantifying
393 tissue-scale mechanical properties and investigating the roles of these properties during the
394 highly complex processes of development and disease progression.

395 Recent advances in stem cell-derived organoid systems have provided a promising new
396 class of biological models for understanding various human pathologies and screening of
397 therapeutic drugs and targets²⁵. While several recently developed materials could function as *in*
398 *vivo* force sensors, long-term *in vivo* imaging of 3D mechanics still remains a challenge due to
399 the large size of these materials, their limited stability and low detection sensitivity in deep
400 tissue^{4,15}. In this study, MGV-based imaging was successfully used to visualize mechanical
401 dynamics of organoids by monitoring the progression of fibrosis and response to anti-fibrotic

402 drugs for long-term. In particular, the ease of grafting MGVs into organoids by microinjection or
403 encapsulation with the lack of toxicity and degradation, empowers a wide range of
404 mechanobiology studies using organoid models of human diseases. As a result, MGV-based
405 measurement of mechanical dynamics may provide novel insights into the roles of
406 mechanobiology in human disease that could be useful in tissue mechanics-based diagnosis and
407 prediction of the best therapeutic outcomes.

408

409 **Methods**

410 **Preparation of magnetic nanoparticles (MNPs)**

411 Zinc-doped iron oxide ($\text{Zn}_{0.4}\text{Fe}_{2.6}\text{O}_4$) nanoparticles were synthesized as previously described²³.
412 Briefly, zinc (II) chloride (ZnCl_2 , $\geq 98\%$, Sigma-Aldrich, USA) and an iron (III) acetylacetonate
413 ($\text{Fe}(\text{acac})_3$, $\geq 98\%$, Sigma-Aldrich, USA) were placed in a three-neck round-bottom flask in the
414 presence of oleic acid (Sigma-Aldrich, USA), oleylamine (Sigma-Aldrich, USA), and octyl ether
415 (98%, Aldrich, USA) under argon gas. Silica coating was used to make these nanoparticles water
416 soluble and functionalizable. To begin, the surface was treated with tetraethyl orthosilicate
417 (Sigma-Aldrich, USA), cyclohexane (Deajung, Korea), IGEPAL CO-520 (Sigma-Aldrich, USA),
418 and ammonium hydroxide solution (28%, Sigma-Aldrich, USA) for 24 h at room temperature.
419 The second layer was coated with 3-aminopropyl trimethoxysilane (Sigma-Aldrich, USA) for 2 h.
420 After separation with tetramethyl ammonium hydroxide (TMAOH, 97%, Aldrich, USA), to
421 introduce azide groups on the surface of the nanoparticles, silica-coated nanoparticles (1 mg)
422 were then coated with m-dPEG12-TFP ester (9 mg, Quanta BioDesign, USA), Azido-dPEG12-
423 TFP ester (1 mg, Quanta BioDesign, USA) in DMSO for 2 h at room temperature. Nanoparticles

424 were isolated using a MidiMACS separator column and were dispersed in 10 mM phosphate
425 buffer (PB) buffer.

426

427 **Preparation of gas vesicles (GVs)**

428 *Anabaena* gas vesicles were obtained as previous method⁵¹. Briefly, GV_s were isolated from
429 *Anabaena flos-aquae* using hypertonic lysis and purified using centrifugally assisted flotation.
430 Stripped GV_s were prepared by treatment with 6 M urea solution followed by an additional
431 centrifugally assisted flotation and removal of the supernatant. To functionalize DBCO on the
432 surface of the GV_s, DBCO-sulfo-NHS ester (Click Chemistry Tool, USA) was mixed with GV_s
433 at a molar ratio of 1:10 in deionized water (DIW) for 4 h at 4°C at 30 rpm in a vertical shaker.
434 Functionalized GV_s were dialyzed in DIW for 72 h with a water exchange every 24 h.

435

436 **Development and characterization of MGVs**

437 Magnetic nanoparticle conjugated GV_s (magneto-GV_s, MGVs) were developed by conjugating
438 MNPs to GV_s at a molar ratio of 1:100 for 4 h at 4°C at 30 rpm in a vertical shaker. After 4 h, the
439 MGVs were purified three times using buoyancy purification at 300 rpm, 4°C, 24 h, and the
440 solvent was replaced with phosphate-buffered saline (PBS) each time. To characterize the
441 morphology, size, and magnetic susceptibility of MGVs, techniques including transmission
442 electron microscopy (TEM, JEOL 2100, JEOL, Japan), dynamic light scattering (DLS, Zetasizer
443 Nano ZS, Malvern, UK), and vibrating sample magnetometer (VSM, Vibration 7407-S, Lake
444 Shore Cryotronics, USA) measurements, respectively, were used. Inductively coupled plasma
445 mass spectrometry (ICPMS, ICAP 7200 Duo + ASX-560, Thermo Fisher Scientific, USA) was

446 used to determine the concentration of MNPs in MGVs. The concentrations of Fe and Zn ions
447 measured by ICP were converted to numbers of MNPs. The concentration of GVs was then
448 calculated by dividing 186 by the average number of MNPs attached to GVs as determined by
449 our TEM images, which was manually calculated (**Supplementary Fig. 3**).

450

451 **Experimental MMUS imaging setup**

452 **Magnet setup.** The schematic illustration of our custom-built MMUS system is illustrated in Fig.
453 1A. A multipurpose DAQ (USB6003, National instruments, USA), power supply (RSP-1000-24,
454 24V, 40A, Meanwell), and solid state module (SSR-40DD, FOTEK) were commercially
455 available. To meet the imaging system requirements, the ultrasound system was modified to
456 output a trigger signal prior to imaging to generate amagnetic field. The magnetic field pulse and
457 strength were controlled by using a customized labview system. The field generator was
458 connected to a coil consisting of mutiple turns with a magnetic coil. To increase the magnetic
459 flux density and to localize the magnetic field in the center of the coil, ferritic stainless steel was
460 embedded. The core size was 5 mm in diameter and 100 mm in height. To better focus the field
461 onto a smaller region of interest, a symmetric conic frustum was cut at 56° on the top side. The
462 magnetic pulse strength, measured at 6 mm above the iron-core tip using a digital gaussmeter
463 (DSP 475, Lakeshore Inc., Westerville, OH), was 0.03 T, which was used for the imaging
464 experiments.

465 **MMUS imaging and processing.** For MMUS imaging, the phantoms were submerged in PBS,
466 and ultrasound images were acquired using a Verasonics Vantage programmable ultrasound
467 scanning system with an L22-14v 128-element linear array transducer with a 0.10-mm pitch, an

468 8-mm elevation focus, a 1.5-mm elevation aperture, and a center frequency of 18.5 MHz with 67%
469 -6 dB bandwidth (Verasonics, Kirkland, WA). Two sets of ultrasound IQ data were collected for
470 *in vitro* and organoid imaging at each loop containing a pulse sequence consisting of 5 tilted
471 plane waves (varying from -6 to 6 degrees), each containing 500 ensemble coherently
472 compounded frames, collected at a framerate of 500 Hz with a voltage of 3V. A total of 20 loops
473 of images were collected per set. The first set was taken as a background frame for background
474 subtraction with the magnetic field off (Mag OFF). The second set was taken with the magnetic
475 field on (Mag ON), during which the function generator was triggered for 2000 μ sec prior to the
476 beginning of the imaging.

477 To obtain each image, IQ data were processed in the same manner as previously described, with
478 quadrature detection used to extract the generated movement based on the excitation frequency⁵².
479 Briefly, for a set of N frames, let $R_I(x, y, n) + jR_Q(x, y, n)$ represent an element in this IQ array
480 with n running from 1 to N, and R_I and R_Q representing the in-phase and quadrature signal,
481 respectively. First, the received IQ data were phase unwrapped to generate a new 3D array
482 $r_{\text{unwrapped}}(x, y, n) = \arg(R_I(x, y, n) + jR_Q(x, y, n))$. Afterward, quadrature detection was used
483 to tease out the signal that oscillates at the magnetic pulse frequency (f_0)

$$484 \quad R(x, y, n) = r_{\text{unwrapped}}(x, y, n) * e^{j2\pi f_0 n \delta t}$$

485 To calculate the displacement amplitude at frequency f_0 for each pixel, all the frames were
486 averaged to calculate $\underline{R(x, y)}$ for the quadrature-detected sequence $R(x, y, n)$. The mean value
487 was used rather than a low-pass filter to determine the displacement amplitude at f_0 , which was
488 obtained as

$$A(x, y) = 2 \left| \underline{R(x, y)} \right| = 2\sqrt{I(x, y)^2 + Q(x, y)^2}$$

489 Finally, ultrasound Delta images were constructed by subtracting the Mag ON frame by the Mag
490 OFF frame. For MMUS signal quantification, the Delta images were used. Regions of interest
491 (ROIs) were defined to capture the ultrasound signal from the phantom well or organoid region.
492 All *in vitro* phantom experiments had the same ROI dimensions. For organoid models, ROIs
493 were selected by B mode images in which the organoid size was not same in all cases.
494 Background ROIs were chosen in areas where no sample was present. The mean pixel intensity
495 was calculated for each ROI, and the signal from the background region and sample region was
496 calculated as the signal to background ratio (SBR).

497

498 **Rheometer measurement**

499 To prepare the hydrogel samples for the rheometer, agarose or Matrigel was solidified at 25 °C or
500 37 °C, respectively, at the desired concentration. The rheometer (Anton Paar MCR102) was set
501 to frequency sweep mode from 100 Hz–0.1 Hz (logarithmic, 16 points) and the (ocillatory) shear
502 strain was set to 1%. Elastic modulus values were determined using the storage modulus
503 obtained at 1 Hz.

504

505 **Ultrasound phantom preparation**

506 ***In vitro* phantom.** To produce *in vitro* MMUS imaging phantoms, wells were cast with molten
507 0.5 % w/v agarose in PBS using a custom 3D-printed template. MGv, MNP, or GV (DBCO-
508 functionalized GV) samples were mixed 1:1 with 50 °C agarose and injected into wells prior to
509 solidification. Matrigel was stored at 4°C until loaded and solidified for 30 minutes at 37 °C.
510 Hydrogels and samples were made at a concentration two times greater than the final required

511 concentration.

512 **Organoid phantom.** For MMUS imaging of organoids, a polydimethylsiloxane (PDMS) mold
513 was fabricated. PDMS solution was prepared by mixing PDMS pre-polymer (Sylgard 184; Dow
514 Corning, Midland, MI, USA) and curing agent (Dow Corning) at a ratio of 10:1 (v/v). Then the
515 mixture was poured into 60 pi petri dishes and cured in a drying oven for 4 h after removing
516 bubbles using a vacuum chamber. The center of the cured PDMS mold was punched to make
517 chambers for the organoids. After sterilizing each PDMS mold with ultraviolet (UV) irradiation
518 for 30 minutes, MGV-microinjected lung organoids or MGV-incorporated liver organoids were
519 encapsulated in growth factor-reduced Matrigel (Corning, Corning, NY, USA) and transferred to
520 the chambers in the mold. After the gelation of Matrigel, the organoids were cultured in growth
521 medium, and MMUS imaging was performed after replacing the medium with 1× phosphate-
522 buffered saline (PBS, Sigma-Aldrich, St. Louis, MO, USA). For fibrosis induction, lung
523 organoids were cultured in medium including recombinant human transforming growth factor
524 (TGF)- β 1 (Peprotech, Rocky Hill, NJ, USA) without A83-01 (Tocris, Bristol, United Kingdom).
525 For the drug tests with lung organoids, 10 μ M nintedanib (Sigma-Aldrich) was administered to
526 the organoids every 2-3 days starting from day 5 after fibrosis induction. Liver organoids were
527 also cultured in medium containing TGF- β 1 for fibrosis induction, and 10 μ M obeticholic acid
528 (OCA, Selleck, USA) used for the drug tests was administered to the organoids every 2-3 days
529 starting from the first day of fibrosis induction (day 0).

530

531 **Organoid experiments**

532 **Generation of lung organoids and MGV microinjection.** Lung organoids were prepared from

533 human lung tissues harvested with the patients' consent. The use of human lung tissues for lung
534 organoid generation was approved by the Institutional Review Board (IRB) of Severance
535 Hospital (IRB No: 4-2021-1555). The basal medium used to isolate lung cells from tissues and to
536 prepare growth medium for lung organoid culture consisted of advanced DMEM/F12
537 (Dulbecco's Modified Eagle Medium/Ham's F-12) containing 2 mM GlutaMax, 10 mM HEPES
538 (N-2-hydroxyethylpiperazine-N-2-ethane sulfonic acid) and 1% (v/v) penicillin/streptomycin
539 (P/S) (all from Thermo Fisher Scientific, Waltham, MA, USA). Then, organoid growth medium
540 was prepared using the basal medium supplemented with 10% (v/v) R-spondin1-conditioned
541 medium, 1× B27 (Thermo Fisher Scientific), 100 ng/mL mouse Noggin (Peprotech), 100 ng/mL
542 human fibroblast growth factor-10 (FGF10, Peprotech), 25 ng/mL human fibroblast growth
543 factor-7 (FGF7, Peprotech), 1.25 mM N-acetyl cysteine (Sigma-Aldrich), 5 mM nicotinamide
544 (Sigma-Aldrich), 500 nM A83-01 (Tocris), and 100 µg/mL primocin (InvivoGen, San Diego, CA,
545 USA). R-spondin1-conditioned medium was prepared using HEK293T cells expressing Rspo1-
546 Fc, which were obtained from Calvin Kuo's laboratory at Stanford University. Lung organoids
547 were generated using a previously reported protocol⁵³. Briefly, harvested human lung tissues
548 were fragmented using scissors, and then washed three times with Dulbecco's phosphate
549 buffered saline (DPBS, Sigma-Aldrich). The tissues were incubated in collagenase type \square (2
550 mg/mL solution in basal medium, Thermo Fisher Scientific) with gentle shaking for 1 h at 37 \square .
551 Digested tissues were then washed with DPBS and strongly pipetted with 0.1% (v/v) fetal bovine
552 serum (FBS, Thermo Fisher Scientific) diluted in DPBS to separate cells from the tissue. The
553 suspension was filtered with a 70 µm strainer to remove the tissue debris, and the number of
554 isolated cells was counted. Then, cells were encapsulated in growth factor-reduced Matrigel at a
555 concentration of 5×10^6 cells/mL and were moved into a 48 well plate. After gelation for 10

556 minutes, growth medium was added to each well. The growth medium was replaced every 3-4
557 days, and 10 μ M Y27632 (BioGems International, Inc., Westlake Village, CA, USA) was added
558 to the culture for the first 4 days. The microinjections of MGVs were performed using a method
559 similar to microinjection into embryos in a previous study⁵⁴. The end of a Pasteur pipette was
560 made narrow for microinjection using an alcohol lamp, and it was connected to a mouthpiece and
561 rubber tubing. MGV solution (OD16) was microinjected into lung organoids, and the organoids
562 were then cultured for 2 days to allow for stabilization. After Matrigel encapsulating the
563 organoids was degraded by treatment with cell recovery solution (Corning), the harvested MGV-
564 microinjected lung organoids were transferred to the organoid chamber of a PDMS mold for
565 MMUS imaging. Microinjection of GVs or MNPs was performed in the same manner as
566 microinjection of MGVs.

567 **Human iPSC maintenance.** A human induced pluripotent stem cell (hiPSC) line (CHO) was
568 kindly provided by the Yonsei University School of Medicine, and the use of hiPSCs for the liver
569 organoid study was approved by the Institutional Review Board (IRB) of Yonsei University
570 (permit number: 7001988-202104-BR-1174-01E, 7001988-202104-BR-1175-01E). The hiPSC
571 line was characterized for pluripotency and regularly checked for mycoplasma contamination.
572 Culture of hiPSCs was performed using StemMACS iPSC-Brew XF medium (Miltenyi Biotec,
573 Bergisch Gladbach, Germany) under Matrigel-coated, feeder-free conditions. Cells were
574 passaged every 5-7 days using ReLeSR (STEMCELL Technologies, Vancouver, BC, Canada)
575 and maintained within passages 20 to 50.

576 **Generation of MGV-incorporated human liver organoids.** For generation of liver organoids,
577 four types of cells (hepatic endodermal cells, hepatic stellate cells, endothelial cells, and
578 mesenchymal cells) were prepared. Hepatic endodermal cells and hepatic stellate cells were

579 differentiated from hiPSCs. Human umbilical vein endothelial cells (HUVECs) and human
580 mesenchymal stem cells (hMSCs) were purchased from Lonza (Basel, Switzerland). The
581 differentiation protocol for hepatic endodermal cells was adapted from the previous methods
582 with slight modifications^{55,56}. Briefly, hiPSCs were seeded on Matrigel-coated 6-well plates with
583 mTeSR plus medium (STEMCELL Technologies) and 10 μ M Y27632. After 24 h, the medium
584 was changed to RPMI 1640 (Thermo Fisher Scientific) and supplemented with 100 ng/mL
585 activin A (R&D Systems, Minneapolis, MN, USA) and 1% B27 minus insulin (Thermo Fisher
586 Scientific), and the cells were cultured for 4 days to induce definitive endodermal cells.
587 CHIR99021 (3 μ M, LC laboratory, Woburn, MA, USA) was added to the medium only on the
588 first day of the 4-day differentiation protocol. Then, the cells were further cultured for an
589 additional 3 days to induce hepatic endodermal cells in RPMI 1640 medium supplemented with 1%
590 B27 (Thermo Fisher Scientific), 20 ng/mL bone morphogenetic protein 4 (BMP4, R&D
591 Systems), and 10 ng/mL fibroblast growth factor-basic (bFGF, Peprotech). The differentiation
592 protocol for hepatic stellate cells was adapted from a previously reported method with slight
593 modifications⁵⁷. Briefly, hiPSCs were seeded on Matrigel-coated 6 well plates with mTeSR Plus
594 medium and 10 μ M Y27632. After 24 h, cells were treated with 20 ng/mL BMP4 in a hepatic
595 stellate cell basal medium composed of 40% (v/v) MCDB201 (Sigma-Aldrich), 57% (v/v)
596 DMEM low-glucose (Thermo Fisher Scientific), 1% (v/v) P/S, 0.1 μ M β -mercaptoethanol
597 (Sigma-Aldrich), 100 μ M L-ascorbic acid (Sigma-Aldrich), 2.5 μ M dexamethasone (Sigma-
598 Aldrich), 0.25 \times insulin-transferrin-selenium supplement (Sigma-Aldrich), and 0.25 \times linoleic
599 acid (Sigma-Aldrich) for 4 days to induce mesodermal progenitors. Cells were further
600 differentiated into mesothelial cells for an additional 4 days. Cells were treated with 20 ng/mL
601 BMP4, 20 ng/mL fibroblast growth factor-acidic (FGF1, Peprotech), and 20 ng/mL fibroblast

602 growth factor-3 (FGF3, R&D Systems) for the first 2 days and with 20 ng/mL FGF1, 20 ng/mL
603 FGF3, 5 μ M retinol (Sigma-Aldrich), and 100 μ M palmitic acid (Sigma-Aldrich) for the
604 remaining 2 days. For the final stage of hepatic stellate cell differentiation, 5 μ M retinol and 100
605 μ M palmitic acid were added to the hepatic stellate cell basal medium for 4 additional days. The
606 growth medium was exchanged every two days. HUVECs were cultured with EGM-2 medium
607 (Lonza), and hMSCs were maintained with mesenchymal stem cell growth medium (MSCGM,
608 Lonza). To generate MGV-incorporated liver organoids, a 4 mg/mL collagen hydrogel containing
609 MGVs was prepared using rat tail collagen type I (Corning). A pre-gel solution for the collagen
610 hydrogel (final concentration: 4 mg/mL) was prepared by mixing the collagen solution with 10%
611 (v/v) 10 \times PBS (Sigma-Aldrich) and 10% (v/v) MGVs ($OD_{500} = 16$). Finally, the pH of the pre-
612 gel solution was adjusted to 7.4 using 0.5 M sodium hydroxide (NaOH, Sigma-Aldrich). After
613 centrifuging a Eppendorf tube containing the four types of cells at a ratio of 10:7:2:2 (hepatic
614 endodermal cell:HUVEC:hMSC:hepatic stellate cell), the supernatant was removed and the pre-
615 gel solution was added for cell resuspension. The final density of total cells was 2×10^7 cells/mL,
616 and 5 μ L of collagen hydrogel was used for the production of one liver organoid. The liver
617 organoids generated in MGV-containing collagen hydrogels were cultured in ultra-low
618 attachment 24-well plates (Corning) using the following medium: basal medium with equal
619 volumes of HCM Bulletkit (Lonza) and EGM-2 medium supplemented with 3% (v/v) FBS, 1%
620 (v/v) P/S, 20 ng/mL HGF (Peprotech), 10 ng/mL Oncostatin-M (ProSpec, Rehovot, Israel), and
621 0.1 μ M dexamethasone.

622 **Immunostaining of organoids.** Whole-mount immunostaining was performed to check the
623 overall protein expression in organoids. First, cultured organoids were fixed with 10% (v/v)
624 formalin (Sigma-Aldrich) for 1 h at room temperature (RT), and then permeabilized with 0.1%

625 (v/v) Triton X-100 (Sigma-Aldrich) for 30 minutes at RT. After blocking samples with 5% (w/v)
626 bovine serum albumin (BSA, MP biomedical, Asse-Relegem, Belgium) solution for 2 h at RT,
627 the organoid samples were incubated with primary antibodies for 24 h at 4 °C. After washing
628 three times with 1× PBS, secondary antibodies were added to the samples for 24 h at 4 °C. After
629 washing three times with 1× PBS, 4',6-diamidino-2-phenylindole (DAPI, TCI Chemicals, Tokyo,
630 Japan) was added to stain the nuclei of the organoids. Separately, immunostaining was performed
631 after sectioning the organoids to more clearly identify the internal organoid structure. To this end,
632 cultured organoids were fixed with 10% (v/v) formalin (Sigma-Aldrich) for 1 h at RT, and then
633 optimal cutting temperature (OCT) blocks containing organoids were prepared using OCT
634 compound (CellPath, Newtown, United Kingdom). After slicing the OCT blocks into sections,
635 they were permeabilized with 0.1% (v/v) Triton X-100 for 10 minutes at RT. After blocking the
636 samples with 5% (w/v) BSA solution for 2 h at RT, they were incubated with primary antibodies
637 overnight at 4 °C. After washing three times with 1× PBS, secondary antibodies were added to the
638 samples for 1 h at RT. After washing three times with 1× PBS, DAPI was added to stain the
639 nuclei of the organoid samples. In this study, the following primary antibodies were used: mouse
640 anti-smooth muscle actin (SMA, Santa Cruz Biotechnology, Inc., Dallas, TX, USA), mouse anti-
641 vimentin (VIM, Sigma-Aldrich), rabbit anti-P63 (Abcam, Cambridge, MA, USA), mouse anti-
642 MUC5AC (Abcam), mouse anti-acetylated α -tubulin (α -tubulin, Santa Cruz Biotechnology, Inc.),
643 and rabbit anti-albumin (ALB, Sigma-Aldrich). The following secondary antibodies were used;
644 Alexa-Fluor 488-conjugated anti-mouse IgG (Thermo Fisher Scientific), Alexa-Fluor 594-
645 conjugated anti-mouse IgG (Thermo Fisher Scientific), and Alexa-Fluor 594-conjugated anti-
646 rabbit IgG (Thermo Fisher Scientific). TRITC-conjugated phalloidin (Sigma-Aldrich) for
647 staining F-actin in the cytoskeleton was added to the samples treated with secondary antibodies.

648 Stained organoids and sections were imaged using a confocal microscope (LSM 900, Carl Zeiss,
649 Jena, Germany).

650

651 **Animal experiments**

652 All *in vivo* experiments were conducted in accordance with a protocol approved by the California
653 Institute of Technology's Institutional Animal Care and Use Committee (IACUC). Throughout
654 all injection and imaging procedures, mice were anesthetized with ~1–2.5 percent isoflurane.
655 Mice were positioned with the liver facing directly upwards. Prior to each experiment,
656 ultrasound gel was centrifuged at $2,000 \times g$ for 10 minutes to remove bubbles, heated to 37°C ,
657 and then carefully applied to the bodies of the mice. To obtain a precise signal, for all *ex vivo* and
658 *in vivo* models, stripped GVs were used. Stripped MGVs were prepared in the same manner as
659 previously described MGVs. The concentration of GVs was matched to the concentration of
660 MGVs. MNP concentration was also matched to the MNP concentration found in the MGVs.

661 ***Ex vivo* imaging.** For *ex vivo* imaging, three C57 mice aged 8 weeks were injected intravenously
662 in the tail vein with 2,280 pM ($\text{OD}_{500} = 20$) of MGVs and were euthanized after 5 minutes. The
663 concentration used for injections was chosen based on prior research. After euthanasia, the liver
664 was harvested for *ex vivo* imaging. For MMUS imaging, the liver was cast in 0.5% w/v agarose
665 in a 100-mm petri dish and was solidified for 10 minutes. After the first series of imaging, the
666 tissue was fixed for 48 h in 10% formalin at 4°C . The second series of *ex vivo* imaging occurred
667 after fixation.

668 **Live animal imaging.** Five 4-week-old C57 mice were intravenously injected with MGVs for *in*
669 *vivo* imaging. The regions of interest were positioned in the liver tissue using B-mode and

670 Doppler anatomical imaging. The concentration used for injections was chosen based on prior
671 research. MMUS imaging was performed before and after the injection of MGVs with the
672 magnetic field on. 2,280 pM (OD 20) of MGVs were injected intravenously via the tail vein, and
673 MMUS images were taken 5 min post-injection.

674 **Fibrosis model.** Prior to the *in vivo* fibrosis experiment, animals were randomized between
675 experimental groups; blinding was not necessary. C57 mice were treated with CCl₄ (1 μL/g body
676 weight, 1:4 dilution with mineral oil, *N* = 7) or with mineral oil alone (1 μL/g body weight, *N* =
677 4) via intraperitoneal injection two times per week for four weeks^{58,59}. After four weeks, the
678 regions of interest were positioned in the liver tissue using B-mode and Doppler imaging.
679 MMUS imaging was performed before and 5 min after injection with the magnetic field on.
680 2,280 pM of MGVs were injected intravenously via the tail vein in the normal and fibrosis model
681 groups. After MMUS imaging, livers were harvested. Fresh tissue was homogenized and used
682 for a hydroxyproline assay (Sigma-Aldrich, USA). Other parts of the tissue were fixed for 24 h
683 in 10% formalin and then submerged in 70% EtOH for storage. Next, the fixed tissue was
684 embedded in paraffin, sectioned, and stained with H&E and Sirius red (Abcam, USA).

685 ***In vivo* ultrasound imaging.** We employed a recently developed method of ultrafast amplitude
686 modulation (uAM) to precisely visualize and quantify ultrasound contrast *in vivo*⁴⁰. Due to the
687 attenuation of applied sound waves caused by the body, we increased the sound pressure to 370
688 kPa with the same Verasonics system using an L22-14v transducer, which did not collapse either
689 MGVs or GV_s⁴⁰. For each loop, the data were collected at a framerate of 350 Hz with a voltage
690 of 6 V (370 kPa). The pulse sequence consisted of four bursts repeated at three different
691 amplitudes with four different polarity patterns (varying from -14 to 14 degrees). Each burst
692 contained 500 ensemble coherently compounded frames. Two sets of images were taken prior to

693 and following injection. The first set was used as a baseline for background subtraction purposes,
694 with the magnetic field activated prior to injection (before). The second set was taken 5 minutes
695 after injection with the magnetic field activated (after), with the function generator triggered
696 2000 μ sec prior to the start of imaging. A total of twenty looped images were collected per set.
697 We removed frames with poor breathing artifacts based on their Doppler images. To obtain *in*
698 *vivo* ultrasound images, the same processing procedures were used as previously described, and
699 ultimately, ultrasound Delta images were constructed by subtracting the after image from the
700 before image. For *in vivo* MMUS signal quantification, the Delta images were used. ROIs were
701 selected consistently to exclude edge effects from the skin. Background ROIs was selected where
702 there was no sample at all. The mean pixel intensity was calculated for each ROI, and the signal
703 from the background region and sample region was calculated as the signal to background ratio
704 (SBR). For the fibrosis experiments, the ratio of the MMUS (SBR) signal to the uAM (SBR)
705 signal was calculated and reported as a softness index.

706

707 **Statistical analysis**

708 Sample sizes were chosen on the basis of preliminary experiments to have sufficient replicates
709 for statistical comparison. Values and statistical comparisons are given in the text.

710

711 **Code availability**

712 MATLAB code is available from the corresponding author upon reasonable request.

713

714 **Acknowledgements**

715 This work was supported by the Institute for Basic Science (IBS-R026-D1). This work was also
716 supported by the National Research Foundation of Korea (NRF) grant funded by the Korea
717 government, the Ministry of Science and ICT (MSIT) (No. 2021R1A2C3004262) and Samsung
718 Research Funding & Incubation Center of Samsung Electronics under Project Number SRFC-
719 TC2003-03. M.G.S. is an Investigator of the Howard Hughes Medical Institute (HHMI).

720 This article is subject to HHMI's Open Access to Publications policy. HHMI Investigators have
721 previously granted a nonexclusive CC BY 4.0 license to the public and a sublicensable license to
722 HHMI in their research articles. Pursuant to those licenses, the author-accepted manuscript of
723 this article can be made freely available under a CC BY 4.0 license immediately upon
724 publication.

725

726 **Contributions**

727 W.-S.K. performed overall *in vitro* and *in vivo* experiments and analyzed data. S.M designed and
728 performed organoid related experiments. S.K.K., Y.H.K., and S.A. supported hiPSC
729 differentiation, MMUS imaging, and hydrogel characterization, respectively. S.K. provided
730 magnetic nanoparticles. H.D. and A.B. performed initial setup and discussions on this research.
731 D.M. provided gas vesicles. J.-H.L. helped initial setup and discussions on this research. S.H.B.
732 and J.G.L. provided lung tissue for the organoid development. M.K. assisted with the design of
733 research and experiment. W.-S.K and M.K. wrote the manuscript with input from all authors. S.-
734 W.C., M.G.S., and J.C. conceived and supervised the project.

735

736 **References**

- 737 1. Martinez-Vidal, L. *et al.* Causal contributors to tissue stiffness and clinical relevance in urology.
738 *Communications Biology* 2021 4:1 **4**, 1–16 (2021).
- 739 2. Lopez, J. I., Mouw, J. K. & Weaver, V. M. Biomechanical regulation of cell orientation and fate. *Oncogene*
740 2008 27:55 **27**, 6981–6993 (2008).
- 741 3. Guimarães, C. F., Gasperini, L., Marques, A. P. & Reis, R. L. The stiffness of living tissues and its
742 implications for tissue engineering. *Nature Reviews Materials* 2020 5:5 **5**, 351–370 (2020).
- 743 4. Lee, W. *et al.* Dispersible hydrogel force sensors reveal patterns of solid mechanical stress in multicellular
744 spheroid cultures. *Nature Communications* 2019 10:1 **10**, 1–14 (2019).
- 745 5. Babu, P. K. V. & Radmacher, M. Mechanics of brain tissues studied by atomic force microscopy: A
746 perspective. *Frontiers in Neuroscience* **13**, 600 (2019).
- 747 6. Ayala, Y. A. *et al.* Rheological properties of cells measured by optical tweezers. *BMC Biophysics* **9**, (2016).
- 748 7. Janmey, P. A., Fletcher, D. A. & Reinhart-King, C. A. Stiffness sensing by cells. *Physiological Reviews* **100**,
749 695–724 (2020).
- 750 8. Gayraud, C. & Borghi, N. FRET-based Molecular Tension Microscopy. *Methods* **94**, 33–42 (2016).
- 751 9. Lekka, M., Gnanachandran, K., Kubiak, A., Zieliński, T. & Zemła, J. Traction force microscopy –
752 Measuring the forces exerted by cells. *Micron* **150**, 103138 (2021).
- 753 10. Schroyen, B., Vlassopoulos, D., van Puyvelde, P. & Vermant, J. Bulk rheometry at high frequencies: a
754 review of experimental approaches. *Rheologica Acta* **59**, 1–22 (2020).
- 755 11. Kabel, J., Edwards, T. E. J., Sharma, A., Michler, J. & Hosemann, P. Direct observation of the elasticity-
756 texture relationship in pyrolytic carbon via in situ micropillar compression and digital image correlation.
757 *Carbon N Y* **182**, 571–584 (2021).
- 758 12. Bruce, M., Kolokythas, O., Ferraioli, G., Filice, C. & O'Donnell, M. Limitations and artifacts in shear-wave
759 elastography of the liver. *Biomedical Engineering Letters* **7**, 81 (2017).
- 760 13. Campàs, O. *et al.* Quantifying cell-generated mechanical forces within living embryonic tissues. *Nat*
761 *Methods* **11**, 183 (2014).
- 762 14. Serwane, F. *et al.* In vivo quantification of spatially-varying mechanical properties in developing tissues. *Nat*
763 *Methods* **14**, 181 (2017).
- 764 15. Mok, S. *et al.* Mapping cellular-scale internal mechanics in 3D tissues with thermally responsive hydrogel
765 probes. *Nature Communications* **11**, (2020).
- 766 16. Farhadi, A., Ho, G. H., Sawyer, D. P., Bourdeau, R. W. & Shapiro, M. G. Ultrasound Imaging of Gene
767 Expression in Mammalian Cells. *Science* **365**, 1469 (2019).
- 768 17. Mantha, S. *et al.* Smart Hydrogels in Tissue Engineering and Regenerative Medicine. *Materials* **12**, (2019).
- 769 18. Sjöstrand, S., Evertsson, M. & Jansson, T. Magnetomotive Ultrasound Imaging Systems: Basic Principles
770 and First Applications. *Ultrasound in Medicine and Biology* vol. 46 2636–2650 (2020).
- 771 19. Levy, B. E. *et al.* Effect of model thrombus volume and elastic modulus on magnetomotive ultrasound signal
772 under pulsatile flow. *IEEE Transactions on Ultrasonics, Ferroelectrics, and Frequency Control* **65**, 1380–
773 1388 (2018).
- 774 20. Sjostrand, S. *et al.* Contrast-enhanced magnetomotive ultrasound imaging (CE-MMUS) for colorectal
775 cancer staging: Assessment of sensitivity and resolution to detect alterations in tissue stiffness. *IEEE*
776 *International Ultrasonics Symposium, IUS 2019-October*, 1077–1080 (2019).

- 777 21. Shapiro, M. G. *et al.* Biogenic gas nanostructures as ultrasonic molecular reporters. *Nature Nanotechnology*
778 **9**, 311–316 (2014).
- 779 22. Bourdeau, R. W. *et al.* Acoustic reporter genes for noninvasive imaging of microorganisms in mammalian
780 hosts. *Nature* **553**, 86–90 (2018).
- 781 23. Kim, J. *et al.* Single-cell mechanogenetics using monovalent magnetoplasmonic nanoparticles. *Nature*
782 *Protocols* **2017 12:9** **12**, 1871–1889 (2017).
- 783 24. Lu, G. J. *et al.* Acoustically modulated magnetic resonance imaging of gas-filled protein nanostructures.
784 *Nature Materials* **2018 17:5** **17**, 456–463 (2018).
- 785 25. Kim, J., Koo, B.-K. & Knoblich, J. A. Human organoids: model systems for human biology and medicine.
786 *Nature Reviews Molecular Cell Biology* **2020 21:10** **21**, 571–584 (2020).
- 787 26. B, H. Mechanical aspects of lung fibrosis: a spotlight on the myofibroblast. *Proc Am Thorac Soc* **9**, 137–147
788 (2012).
- 789 27. Kang, H. J. *et al.* Cereblon contributes to the development of pulmonary fibrosis via inactivation of
790 adenosine monophosphate-activated protein kinase $\alpha 1$. *Experimental & Molecular Medicine* **2021 53:5** **53**,
791 885–893 (2021).
- 792 28. Meng, X., Nikolic-Paterson, D. J. & Lan, H. Y. TGF- β : the master regulator of fibrosis. *Nature Reviews*
793 *Nephrology* **2016 12:6** **12**, 325–338 (2016).
- 794 29. E, S. *et al.* TLR4 enhances TGF-beta signaling and hepatic fibrosis. *Nat Med* **13**, 1324–1332 (2007).
- 795 30. HR, J. *et al.* Basal cells of the human airways acquire mesenchymal traits in idiopathic pulmonary fibrosis
796 and in culture. *Lab Invest* **95**, 1418–1428 (2015).
- 797 31. Wollin, L. *et al.* Mode of action of nintedanib in the treatment of idiopathic pulmonary fibrosis. *European*
798 *Respiratory Journal* **45**, 1434–1445 (2015).
- 799 32. Chen, G. *et al.* Matrix mechanics as regulatory factors and therapeutic targets in hepatic fibrosis.
800 *International Journal of Biological Sciences* **15**, 2509–2521 (2019).
- 801 33. Lachowski, D. *et al.* Matrix stiffness modulates the activity of MMP-9 and TIMP-1 in hepatic stellate cells
802 to perpetuate fibrosis. *Scientific Reports* **2019 9:1** **9**, 1–9 (2019).
- 803 34. Daley, W. P., Peters, S. B. & Larsen, M. Extracellular matrix dynamics in development and regenerative
804 medicine. *J Cell Sci* **121**, 255–264 (2008).
- 805 35. Bonnans, C., Chou, J. & Werb, Z. Remodelling the extracellular matrix in development and disease. *Nature*
806 *Reviews Molecular Cell Biology* **2014 15:12** **15**, 786–801 (2014).
- 807 36. Margagliotti, S. *et al.* Role of metalloproteinases at the onset of liver development. *Development, Growth &*
808 *Differentiation* **50**, 331–338 (2008).
- 809 37. Roeb, E. Matrix metalloproteinases and liver fibrosis (translational aspects). *Matrix Biol* **68–69**, 463–473
810 (2018).
- 811 38. Radbill, B. D. *et al.* Loss of matrix metalloproteinase-2 amplifies murine toxin-induced liver fibrosis by
812 upregulating collagen I expression. *Dig Dis Sci* **56**, 406–416 (2011).
- 813 39. Maresca, D., Sawyer, D. P., Renaud, G., Lee-Gosselin, A. & Shapiro, M. G. Nonlinear X-Wave Ultrasound
814 Imaging of Acoustic Biomolecules. *Physical Review X* **8**, (2018).
- 815 40. Rabut, C. *et al.* Ultrafast amplitude modulation for molecular and hemodynamic ultrasound imaging.
816 *Applied Physics Letters* **118**, (2021).

- 817 41. Ling, B. *et al.* Biomolecular Ultrasound Imaging of Phagolysosomal Function. *ACS Nano* **14**, 12210–12221
818 (2020).
- 819 42. Ling, Y. *et al.* Effects of fixation and preservation on tissue elastic properties measured by quantitative
820 optical coherence elastography (OCE). *J Biomech* **49**, 1009–1015 (2016).
- 821 43. Chen, Q., Song, H., Yu, J. & Kim, K. Current Development and Applications of Super-Resolution
822 Ultrasound Imaging. *Sensors (Basel)* **21**, (2021).
- 823 44. Delire, B., Stärkel, P. & Leclercq, I. Animal Models for Fibrotic Liver Diseases: What We Have, What We
824 Need, and What Is under Development. *Journal of Clinical and Translational Hepatology* **3**, 53 (2015).
- 825 45. Georges, P. C. *et al.* Increased stiffness of the rat liver precedes matrix deposition: implications for fibrosis.
826 *Am J Physiol Gastrointest Liver Physiol* **293**, 1147–1154 (2007).
- 827 46. Yeh, W. C. *et al.* Elastic modulus measurements of human liver and correlation with pathology. *Ultrasound*
828 *Med Biol* **28**, 467–474 (2002).
- 829 47. Aubé, C. *et al.* [Diagnosis and quantification of hepatic fibrosis with diffusion weighted MR imaging:
830 preliminary results]. *J Radiol* **85**, 301–306 (2004).
- 831 48. Wells, R. G. Tissue mechanics and fibrosis. *Biochimica et Biophysica Acta - Molecular Basis of Disease* vol.
832 1832 884–890 (2013).
- 833 49. Lakshmanan, A. *et al.* Acoustic biosensors for ultrasound imaging of enzyme activity. *Nature Chemical*
834 *Biology* 2020 16:9 **16**, 988–996 (2020).
- 835 50. Vargas, G. *et al.* Applications of Magnetotactic Bacteria, Magnetosomes and Magnetosome Crystals in
836 Biotechnology and Nanotechnology: Mini-Review. *Molecules* □: *A Journal of Synthetic Chemistry and*
837 *Natural Product Chemistry* **23**, (2018).
- 838 51. Lakshmanan, A. *et al.* Preparation of biogenic gas vesicle nanostructures for use as contrast agents for
839 ultrasound and MRI. *Nature Protocols* **12**, 2050–2080 (2017).
- 840 52. Evertsson, M. *et al.* Frequency-and phase-sensitive magnetomotive ultrasound imaging of
841 superparamagnetic iron oxide nanoparticles. *IEEE Transactions on Ultrasonics, Ferroelectrics, and*
842 *Frequency Control* **60**, 481–491 (2013).
- 843 53. Sachs, N. *et al.* Long-term expanding human airway organoids for disease modeling. *The EMBO Journal* **38**,
844 e100300 (2019).
- 845 54. C, L., W, X., C, G. & Y, D. Pronuclear microinjection and oviduct transfer procedures for transgenic mouse
846 production. *Methods Mol Biol* **1027**, 217–232 (2013).
- 847 55. T, T. *et al.* Massive and Reproducible Production of Liver Buds Entirely from Human Pluripotent Stem Cells.
848 *Cell Rep* **21**, 2661–2670 (2017).
- 849 56. Takebe, T. *et al.* Vascularized and functional human liver from an iPSC-derived organ bud transplant. *Nature*
850 *2013 499:7459* **499**, 481–484 (2013).
- 851 57. M, C. *et al.* Generation of Hepatic Stellate Cells from Human Pluripotent Stem Cells Enables In Vitro
852 Modeling of Liver Fibrosis. *Cell Stem Cell* **23**, 101-113.e7 (2018).
- 853 58. Wu, B. M., Liu, J. da, Li, Y. H. & Li, J. Margatoxin mitigates CCl₄-induced hepatic fibrosis in mice via
854 macrophage polarization, cytokine secretion and STAT signaling. *Int J Mol Med* **45**, 103–114 (2020).
- 855 59. Scholten, D., Trebicka, J., Liedtke, C. & Weiskirchen, R. The carbon tetrachloride model in mice.
856 *Laboratory Animals* **49**, 4–11 (2015).

857
858
859
860
861
862
863
864
865
866
867
868
869
870
871
872
873

874 **Figure legends**

875 **Figure 1. Development and characterization of MMUS imaging system and magnetic**
876 **nanoparticle-conjugated GVs (magneto-GVs, MGVs).** (a) Schematic illustration showing the
877 setup and working principle of the MGV-based MMUS imaging system. (b) Schematic
878 illustration of conjugating magnetic nanoparticles (MNPs) to GVs using click chemistry to form
879 MGVs. (c) TEM image of fabricated MGVs (scale bar = 2 μ m, 200 nm). (d) Images of MGVs
880 and GVs after buoyancy purification. (e) The hydrodynamic size of MGVs, MNPs, and GVs
881 with functionalized DBCO by dynamic light scattering (DLS). (f) The magnetic moment of
882 MGVs and MNPs measured by a vibrating-sample magnetometer (VSM). (g) Comparison of
883 MMUS imaging between MGVs, GVs, and MNPs in 0.1% (w/v) agarose phantom using 0.4 nM
884 MGVs, where 0.4 nM MGVs represents 456 pM of GVs and 76 nM of MNPs ($N = 4$
885 independent samples). (h) Magnetic strength-dependent MMUS images and quantification
886 obtained from 7 mT to 30 mT using 0.4 nM MGVs ($N = 3$ independent samples). (i)
887 Concentration-dependent MMUS images and quantification of different groups ($N = 3$
888 independent samples). (j-l) Signal to background ratio (SBR) quantification of MMUS images
889 from different cohorts (j), with varying magnetic strength (k) and concentration (l) for the same
890 conditions as in (g-i). For (g-i) scale bars represent 1 mm. Min and max on color bars represent 0
891 and 10000 arbitrary units, respectively. For (j-l) error bars represent \pm SEM, and significance
892 was determined using one-way ANOVA with Tukey's multiple comparisons test (j) and the

893 multiple unpaired t-test (k, l) ; *: $p < 0.05$; **: $p < 0.01$; ***: $p < 0.001$; ****: $p < 0.0001$.

894

895

896 **Figure 2. Stiffness-dependent MMUS imaging.** (a) Schematic illustration showing the
897 movement of MGVs inside soft and stiff materials when an applied magnetic field is off and on.
898 (b-c) MMUS images and SBR quantification of agarose concentration-dependent movement of
899 MGVs ranging from 0.1% to 0.5% (w/v) agarose ($N = 4$ independent samples). (d-e) MMUS
900 images and SBR quantification based on different values of elastic modulus and concentration (N
901 = 5 independent samples). All scale bars represent 1 mm. Min and max on color bars represent 0
902 and 10000 arbitrary units, respectively. Error bars represent \pm SEM, and significance was
903 determined using the multiple unpaired t-test; *: $p < 0.05$; **: $p < 0.01$; ***: $p < 0.001$; ****:
904 $p < 0.0001$.

905

906 **Figure 3. MGV-based MMUS imaging for monitoring fibrosis in human lung organoid**
907 **model.** (a) Schematic illustration showing microinjection of MGVs into a lung organoid and
908 detection of a change in stiffness in a fibrosis lung organoid using MGVs (scale bar = 0.5 mm).
909 (b) Bright-field images and fluorescence merged images of lung organoids microinjected with
910 GVs and MGVs conjugated with Alexa Fluor 594 and Alexa Fluor 488, respectively (scale bars
911 = 200 μ m). (c) Bright-field, B mode, and MMUS images of lung organoids microinjected with
912 MNPs, GVs, and MGVs (left panel, scale bars = 0.5 mm) and quantification of the signal to
913 background ratio (SBR) of MMUS images in each group (right panel, $N = 6$). (d) Experimental
914 timeline of the preparation of MGV-microinjected lung organoid models and MMUS imaging. (e)
915 Bright-field, B mode, and MMUS images of MGV-microinjected lung organoids (normal
916 organoid model and fibrosis organoid models treated with 10 or 50 ng/mL TGF- β 1). Images
917 were taken from day 5 to day 16 after fibrosis induction (scale bars = 0.5 mm). (f) Quantification
918 of relative SBR signal normalized to the day 5 SBR signal from MMUS images in normal and
919 fibrosis organoid groups ($N = 3$). (g) Hematoxylin & eosin (H&E) staining of organoid sections
920 in normal and fibrosis groups (scale bars = 100 μ m and 50 μ m in left and right images of each
921 group, respectively). Red arrows indicate the localization of MGVs in the organoids. (h) Bright-
922 field, B mode, and MMUS images of MGV-microinjected lung organoids in the normal group,
923 fibrosis group (50 ng/mL TGF- β 1), and drug-treated fibrosis group (50 ng/mL TGF- β 1 + 10 μ M
924 nintedanib). Images were taken from day 5 to day 13 after fibrosis induction (scale bars = 0.5
925 mm). (i) Quantification of relative SBR signal normalized to the day 5 SBR signal from MMUS
926 images in normal, fibrosis, and drug-treated fibrosis groups ($N = 7$). All MMUS images in this
927 Figure were obtained using a scale between 0 and 20000 arbitrary units. Error bars represent \pm
928 standard deviation (SD), and significance was determined using one-way ANOVA with Tukey's
929 multiple comparisons test in (c, f, i); *: $p < 0.05$; **: $p < 0.01$; ***: $p < 0.001$.

930

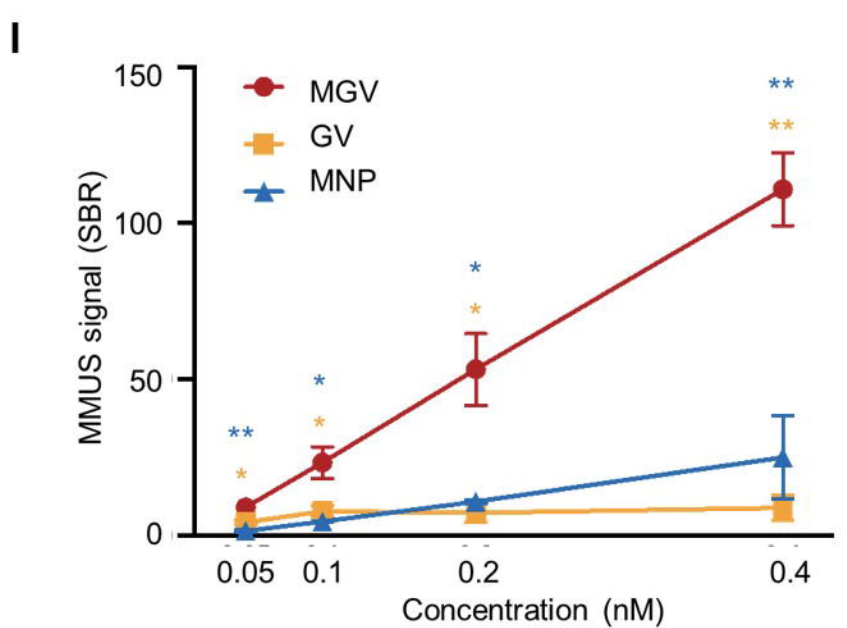
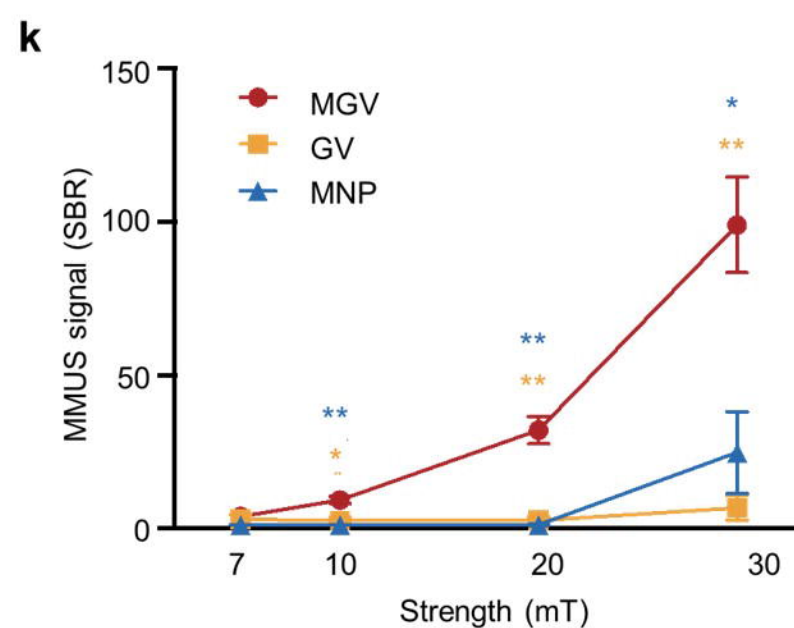
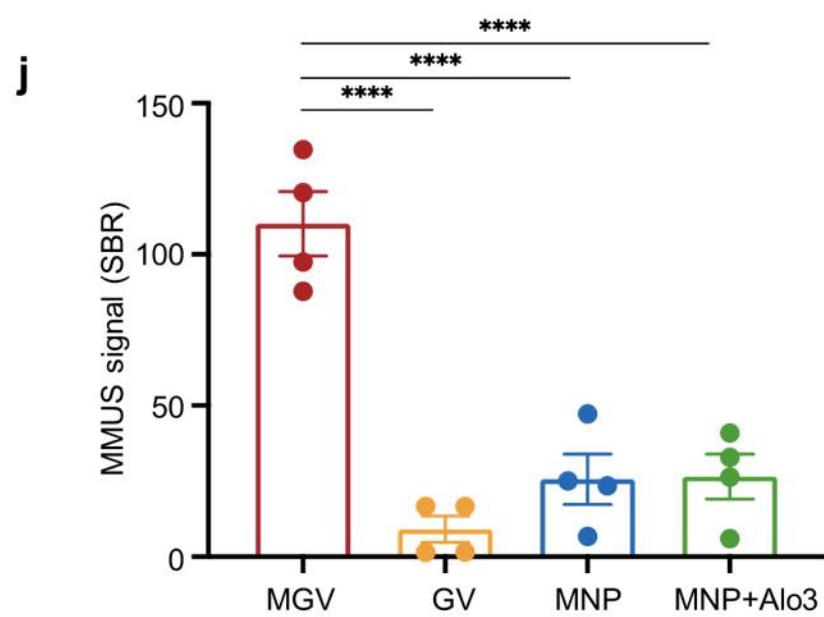
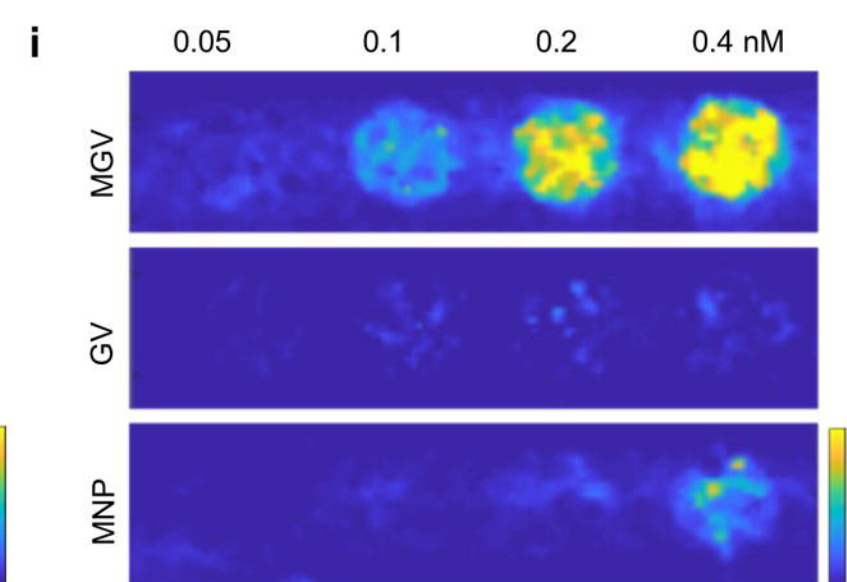
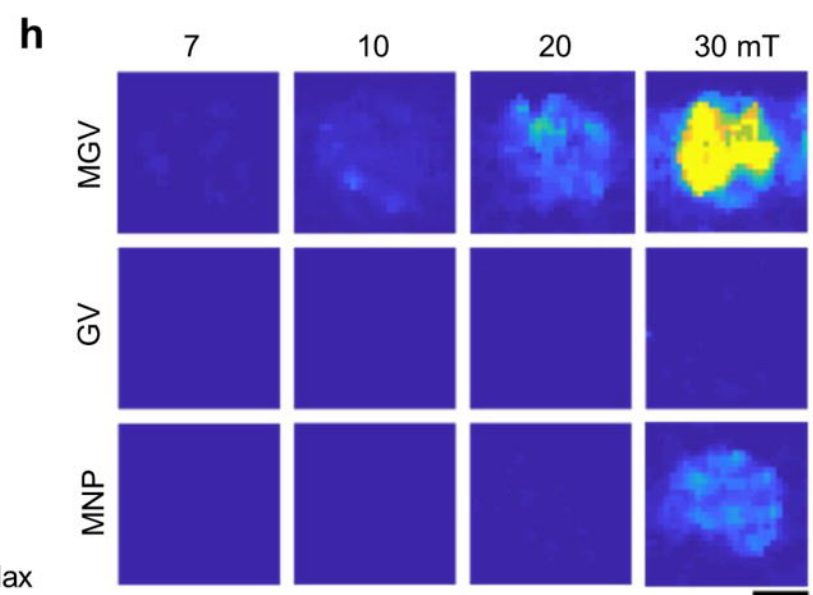
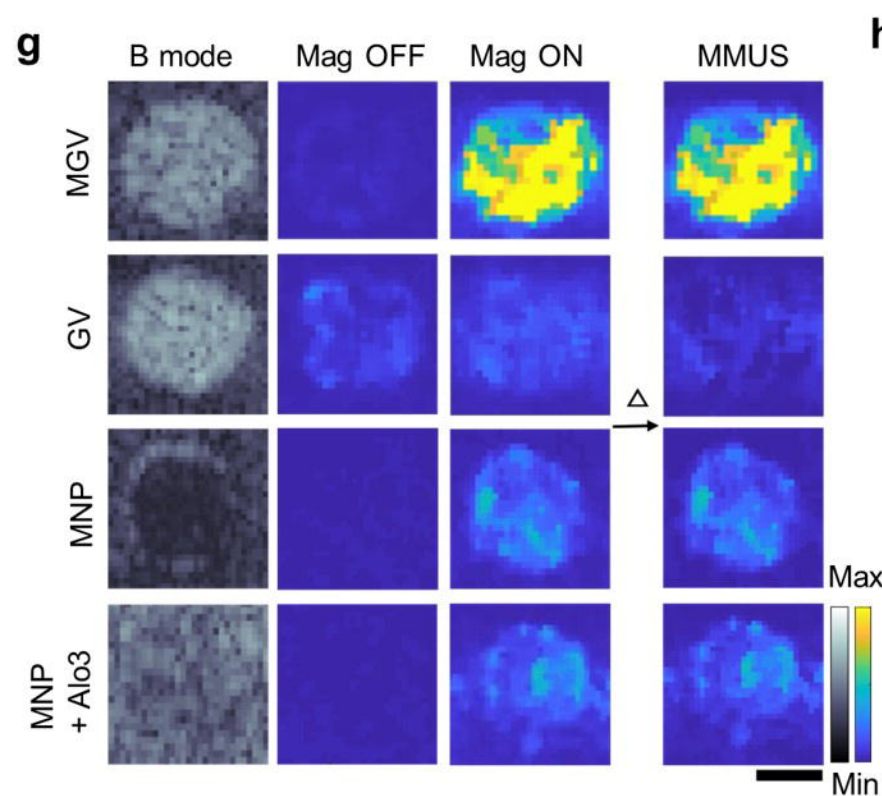
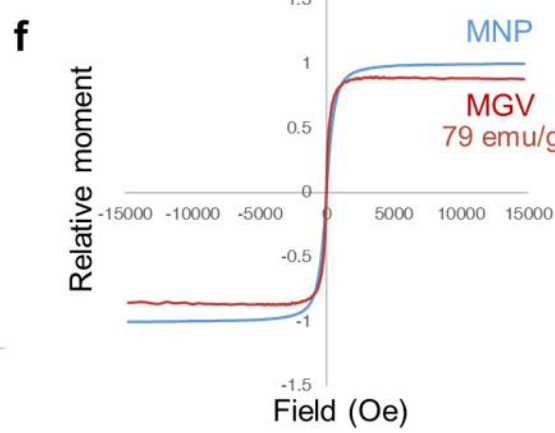
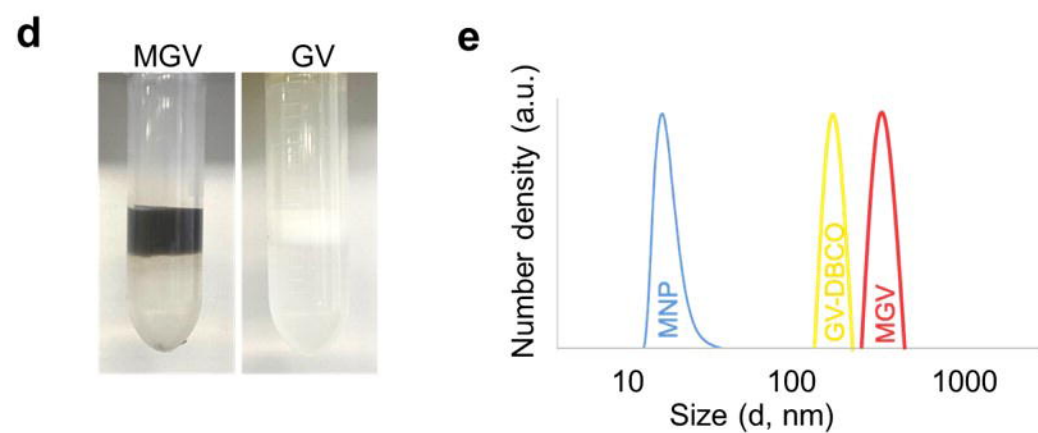
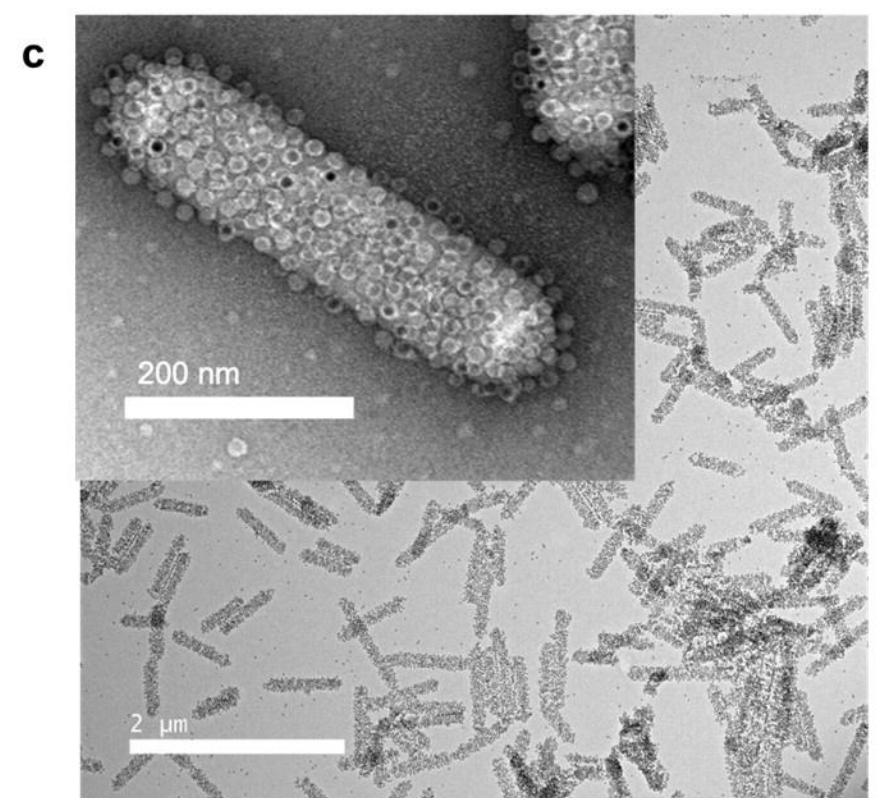
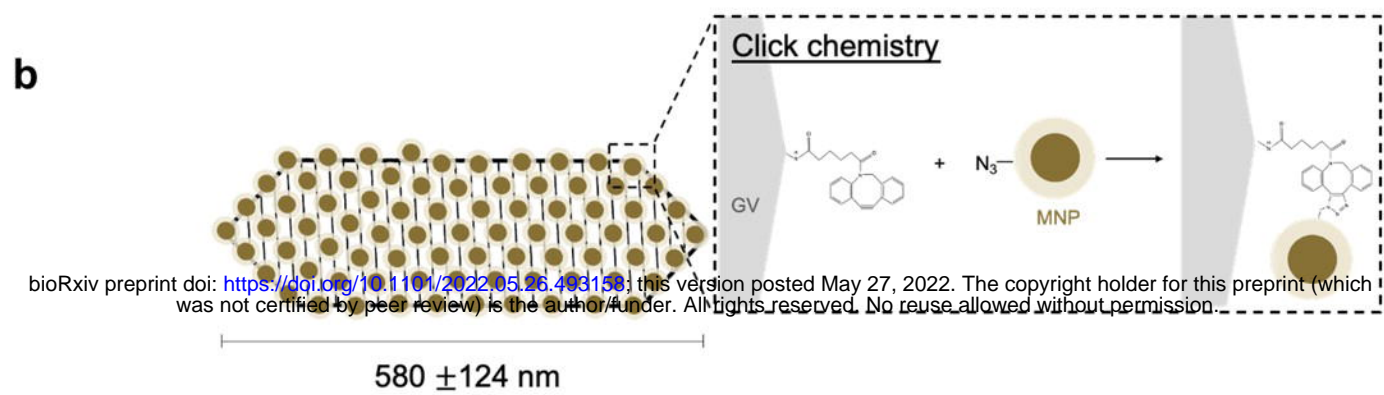
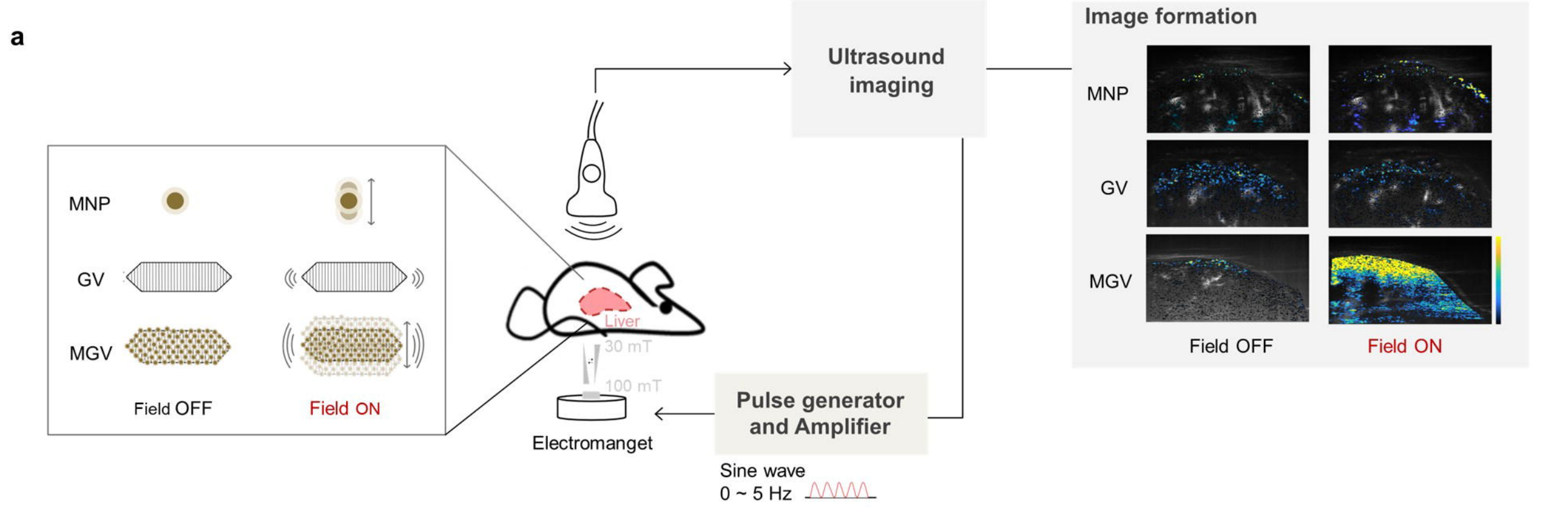
931 **Figure 4. MGV-based MMUS imaging for monitoring fibrosis in human liver organoid**
932 **models.** (a) Schematic illustration showing encapsulation of MGV with four types of cells to
933 generate MGV-incorporated liver organoids and detection of changes in stiffness in fibrosis liver
934 organoids using MGVs. (b) Immunofluorescent images showing the expression of hepatic
935 endodermal cell markers (AFP and ALB) and hepatic stellate cell markers (PDGFRB, GFAP) in
936 liver organoids 3 days after organoid generation. TRITC-conjugated phalloidin was used for
937 cytoskeleton (F-actin) staining and DAPI was used for nuclear staining (scale bars = 200 μ m and
938 20 μ m in the left and right images, respectively). The stained signals were presented in pseudo

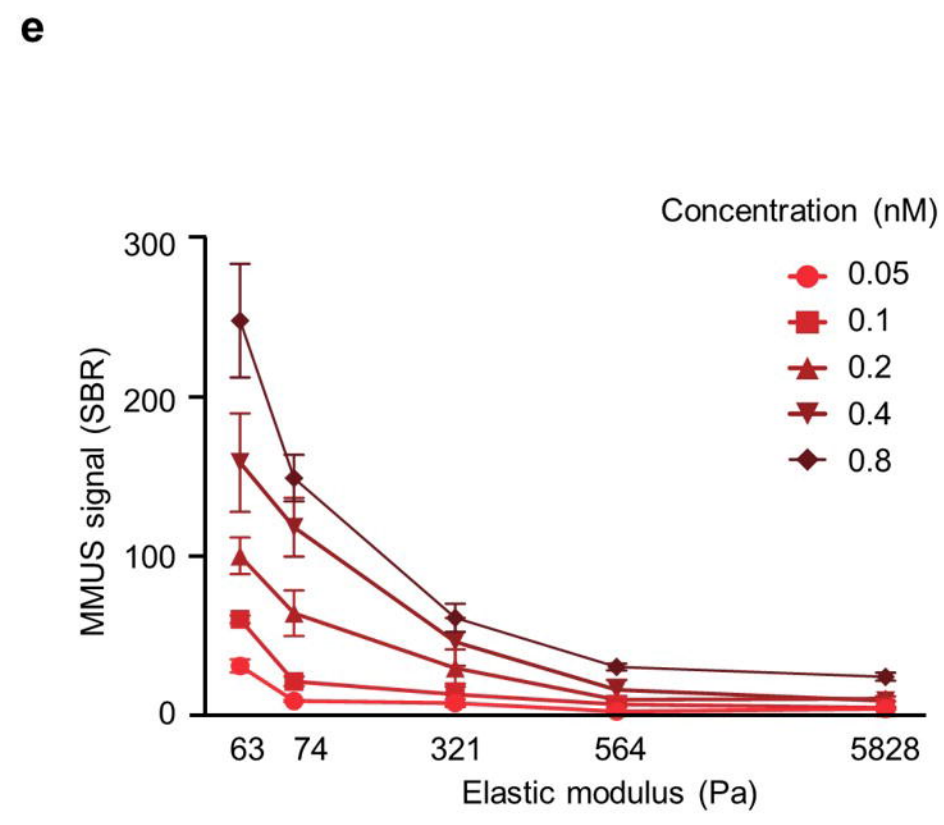
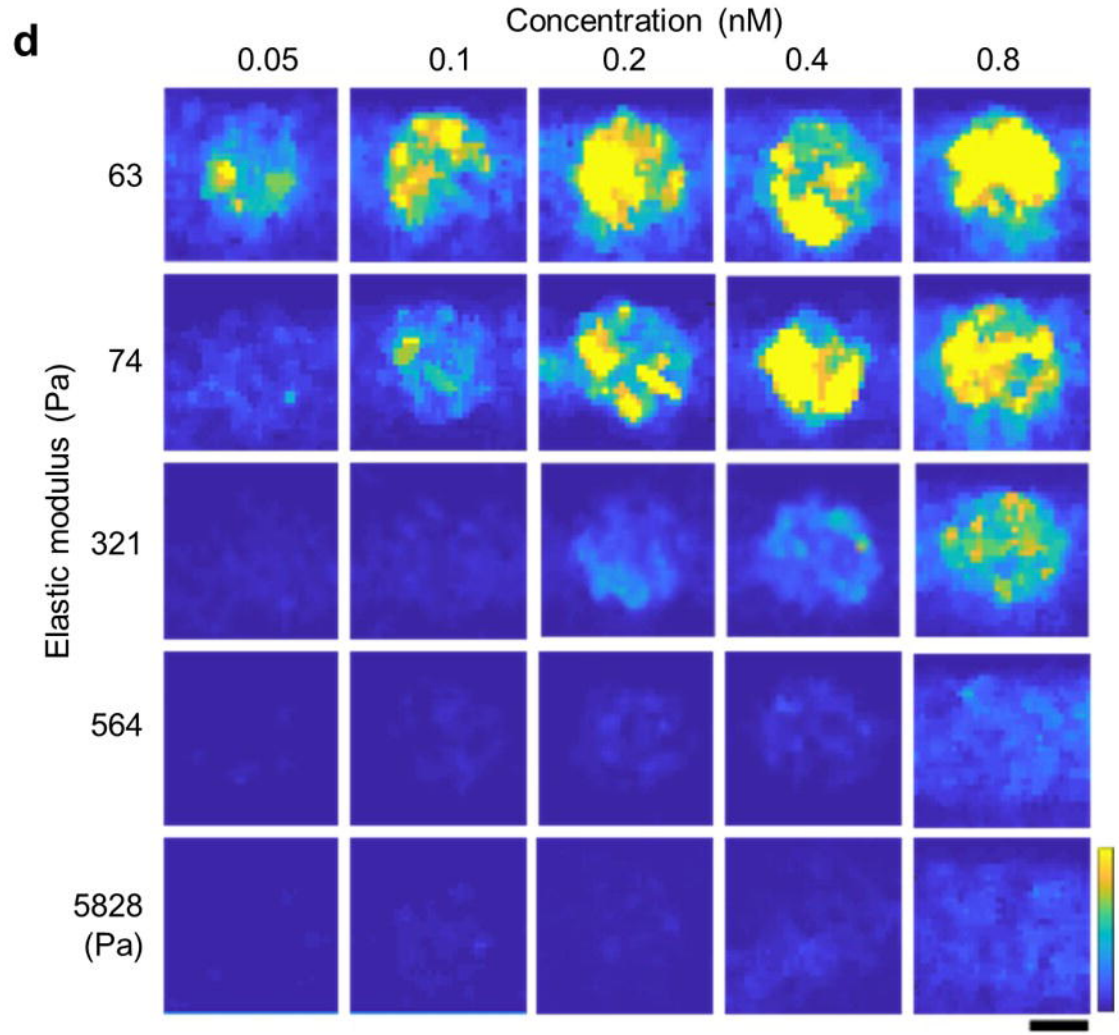
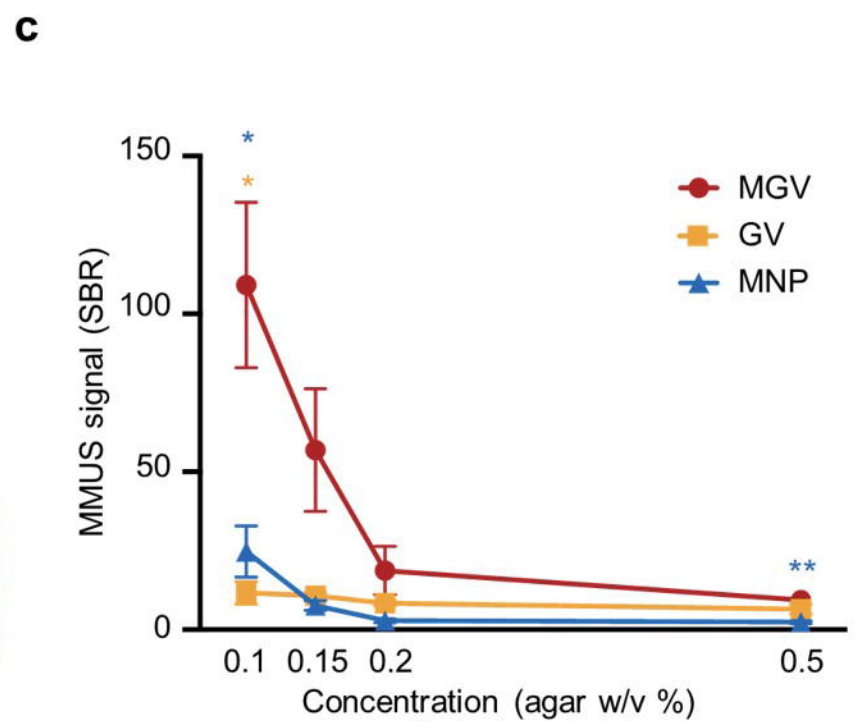
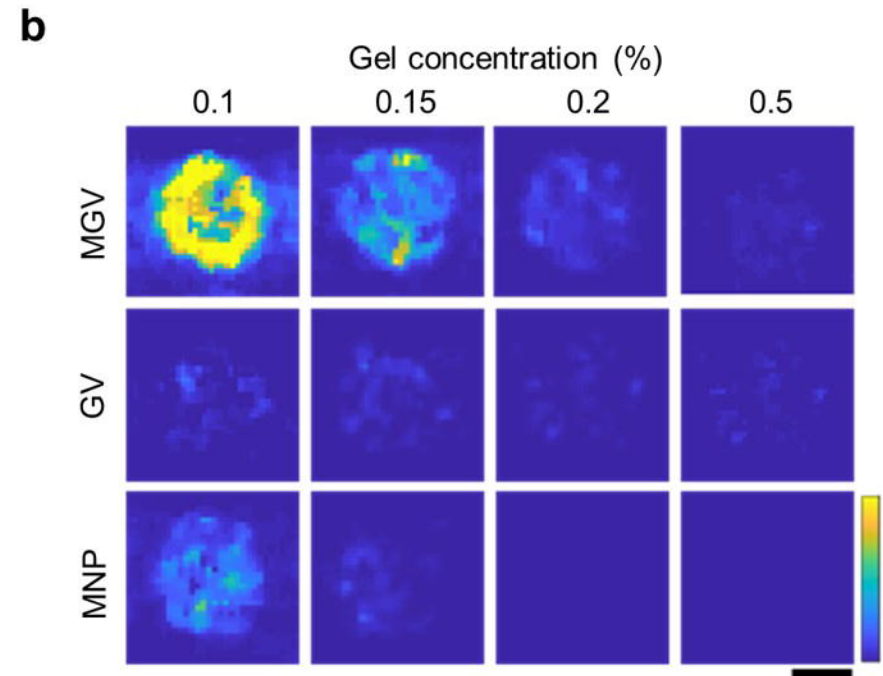
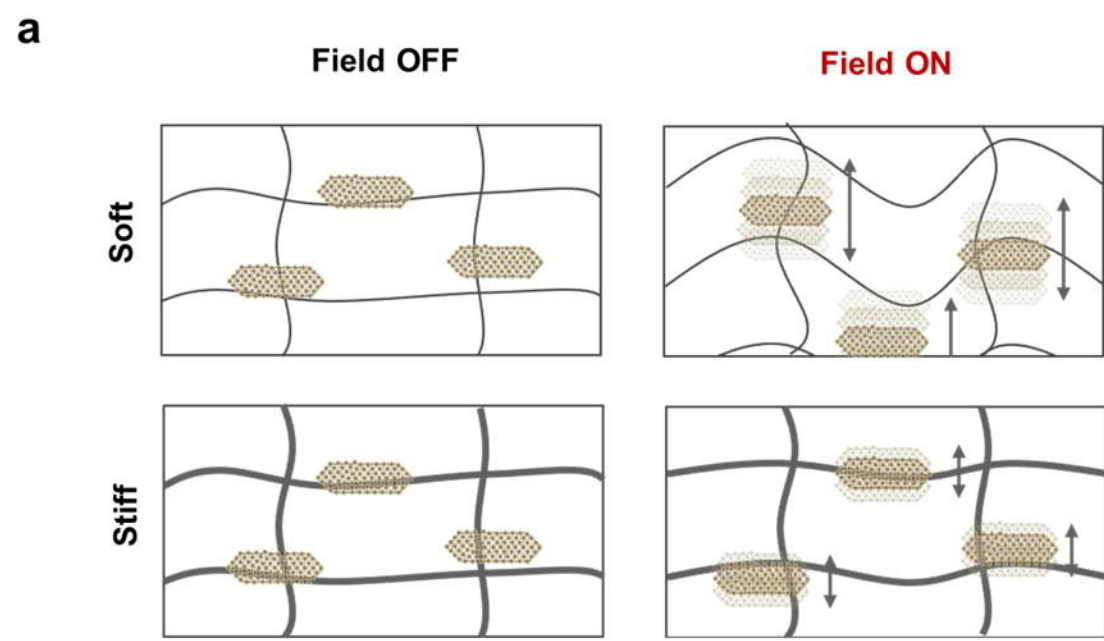
939 color. (c) Experimental timeline of the preparation of MGV-incorporated liver organoid models
940 and MMUS imaging. (d) Bright-field, B mode, and MMUS images of MGV-incorporated liver
941 organoids (normal organoid model and fibrosis organoid model treated with 50 ng/mL TGF- β 1).
942 Images were taken from day 0 to day 7 after fibrosis induction (scale bars = 0.5 mm). (e)
943 Quantification of the relative signal to background ratio (SBR) normalized to the initial signal
944 from MMUS images taken on day 0 in normal and fibrosis organoid groups ($N = 4$). (f)
945 Hematoxylin & eosin (H&E) staining of organoid sections in normal and fibrosis groups (scale
946 bars = 200 μ m and 20 μ m in the left and right images of each group, respectively). Red arrows
947 indicate the localization of MGVs in the organoids. (g) Immunofluorescent images of fibrotic
948 marker (VIM) and mature hepatic marker (ALB) in normal and fibrosis groups. DAPI was used
949 for nuclear staining (scale bars = 500 μ m and 200 μ m in the left and right images of each group,
950 respectively). (h) Bright-field, B mode, and MMUS images of MGV-incorporated liver
951 organoids in the fibrosis group (50 ng/mL TGF- β 1) and drug-treated fibrosis group (50 ng/mL
952 TGF- β 1 + 10 μ M obeticholic acid). Images were taken from day 0 to day 7 after fibrosis
953 induction (scale bars = 0.5 mm). (i) Quantification of the relative SBR normalized to the initial
954 signal from MMUS images taken on day 0 in fibrosis and drug-treated fibrosis groups ($N = 3$).
955 All MMUS images in this Figure were obtained using a scale between 0 and 20000 arbitrary
956 units. Error bars represent \pm standard deviation (SD), and significance was determined using the
957 unpaired two-sided t -test in (e, i); *: $p < 0.05$; **: $p < 0.01$.

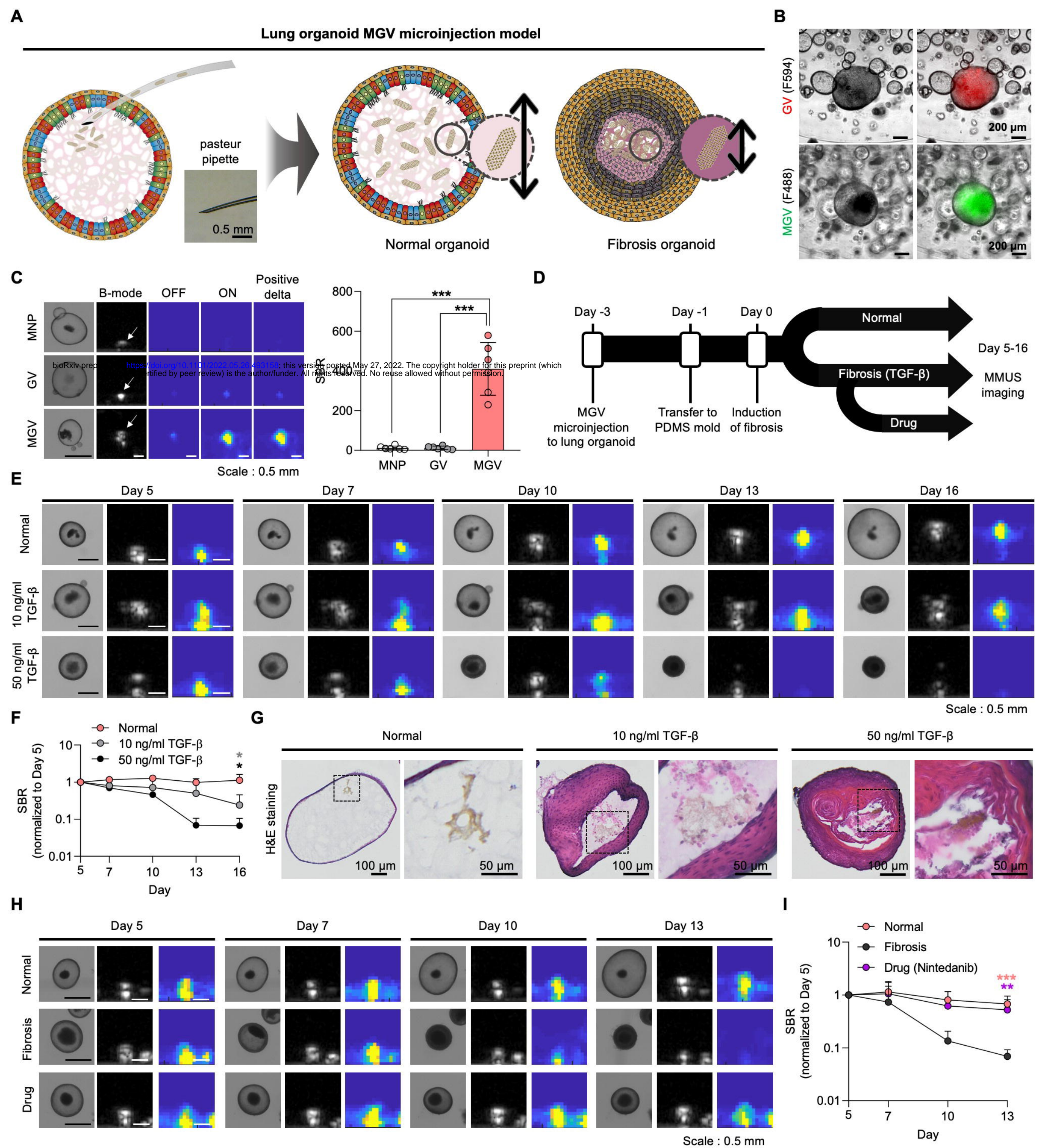
958
959 **Figure 5. MGV-based MMUS imaging in mouse liver.** (a) Experimental scheme of *ex vivo*
960 liver MMUS imaging. (b-c) *Ex vivo* liver MMUS imaging and SBR quantification before and
961 after fixation. MGVs, GVs, or MNPs were injected into the tail vein of mice, and the liver was
962 extracted 5 min after the initial injection. After the first round of imaging, the liver was fixed
963 with 10% formalin for 48 h and imaged again ($N = 3$). (d) Experimental scheme of *in vivo* liver
964 MMUS imaging. (e-f) *In vivo* live animal liver MMUS imaging and SBR quantification. Three
965 different nanomaterials (MGVs, GVs, or MNPs) were injected i.v. and MMUS images were
966 taken after 5 min. B mode images reveal the position of the liver, AM images show the GV
967 signal inside the liver, and Delta MMUS images (parula scale) were overlapped with Doppler
968 images (gray scale) to show the signal below the skin ($N = 5$). All scale bars represent 5 mm. For
969 (b) the color bar represents between 0 and 10000 arbitrary units, and for (e) the min and max on
970 parula and hot color bars represent between 0 and 500000 arbitrary units, respectively, and gray
971 scale bar represents between 0 and 1000000 arbitrary units. Error bars represent \pm SEM, and
972 significance was determined using two-tailed heteroscedastic t -tests with Welch's correction
973 within each group (c) and one-way ANOVA with Tukey's multiple comparisons. *: $p < 0.05$; **: $p < 0.01$;
974 ***: $p < 0.001$; ****: $p < 0.0001$.

975
976
977 **Figure 6. MGV-based MMUS imaging for *in vivo* fibrosis detection.** (a) Experimental
978 timeline of inducing liver fibrosis in a mouse model. Either CCl₄ or mineral oil at a volume of
979 0.1 μ L/g per mouse body weight was injected intraperitoneally twice a week for up to four weeks.
980 (b-c) Ultrasound images and quantification of normal and fibrosis cohorts. The B mode images
981 reveal the position of the liver, AM images show the GV signal inside the liver, and the Delta
982 MMUS images (purula) were overlapped with Doppler images (gray scale) to show the signal
983 below the skin ($N = 4$ for normal group, $N = 7$ for fibrosis group, scale bar = 5 mm). (d) Low-
984 magnification (left) and high-magnification (right) images of H&E stained sections in two

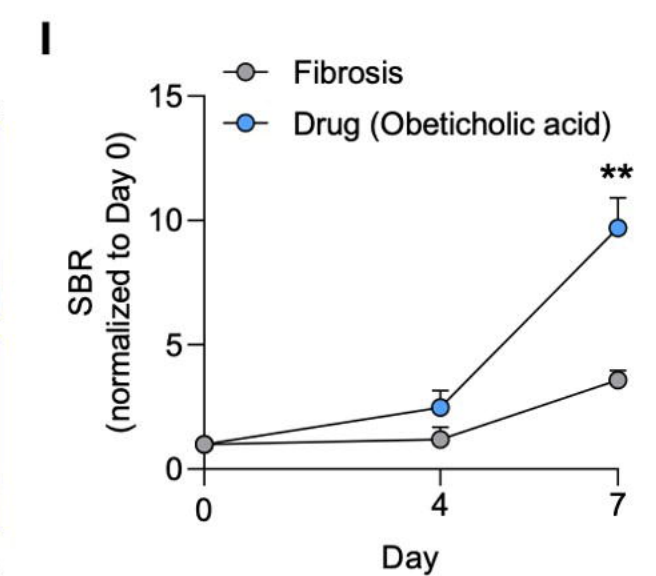
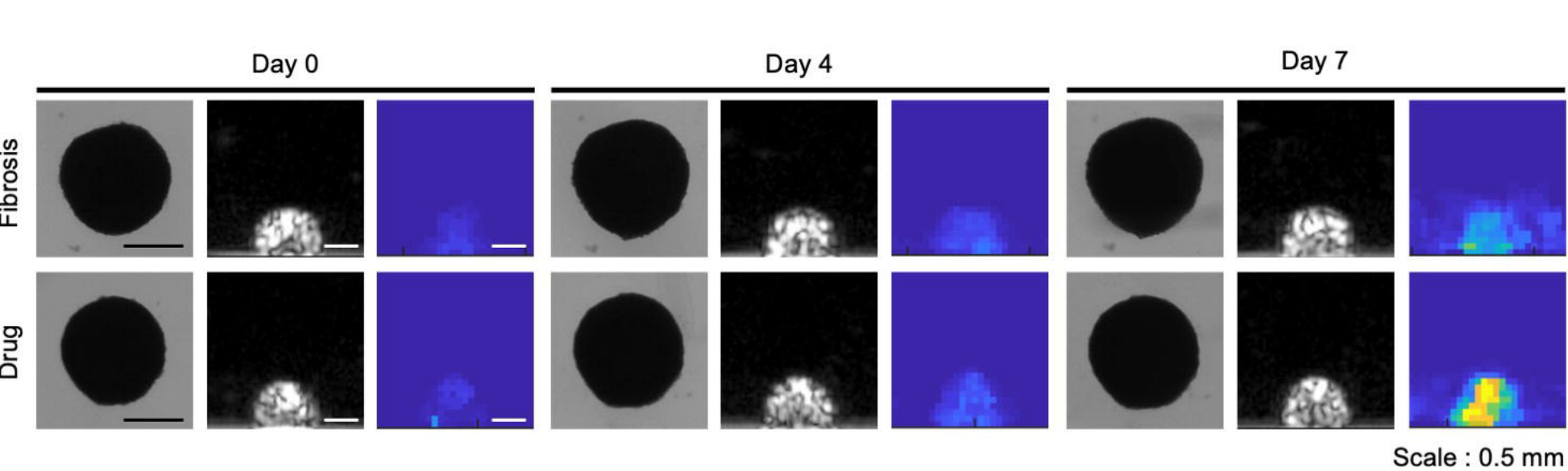
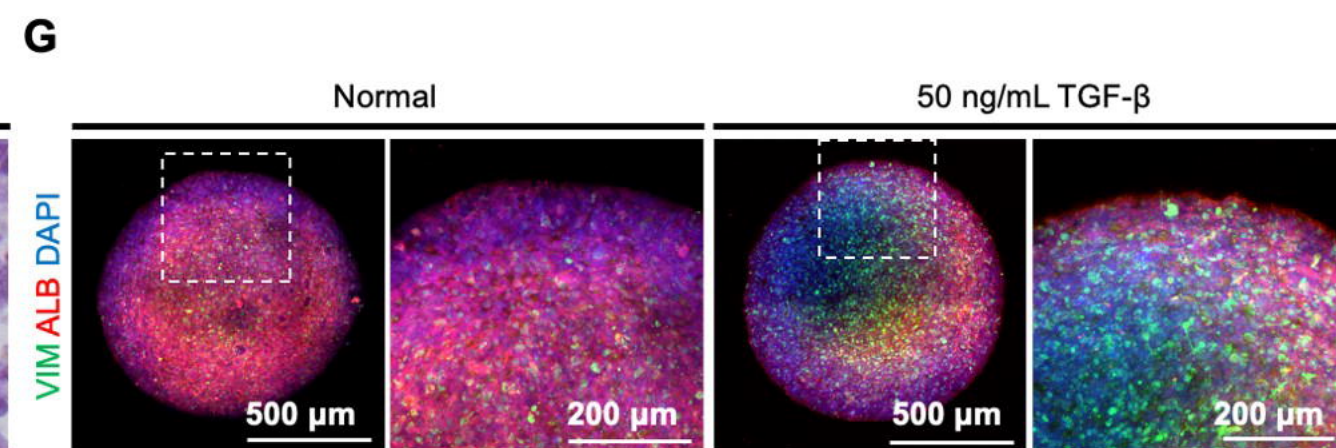
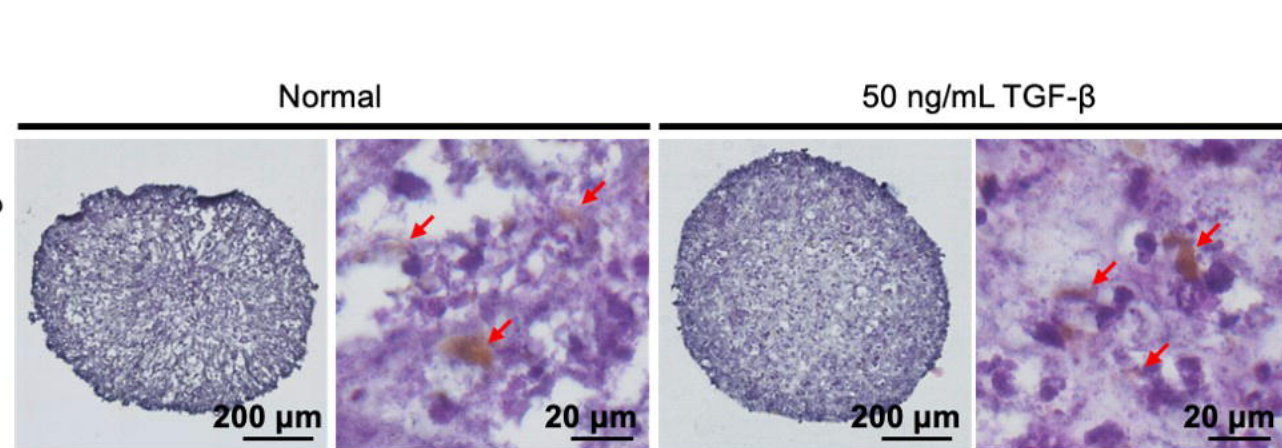
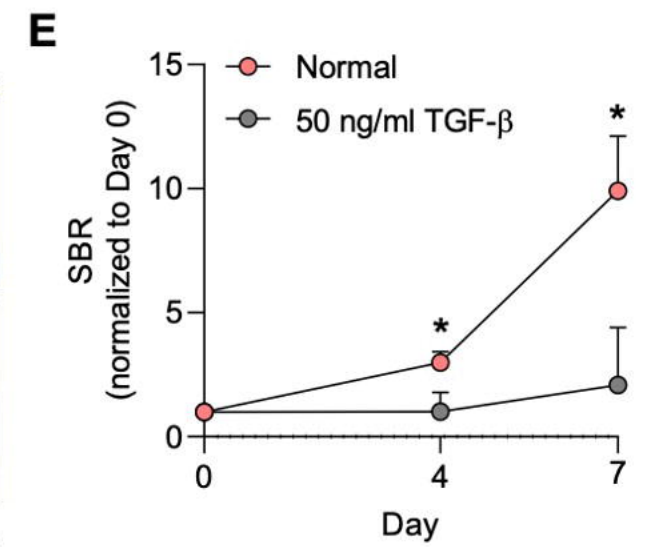
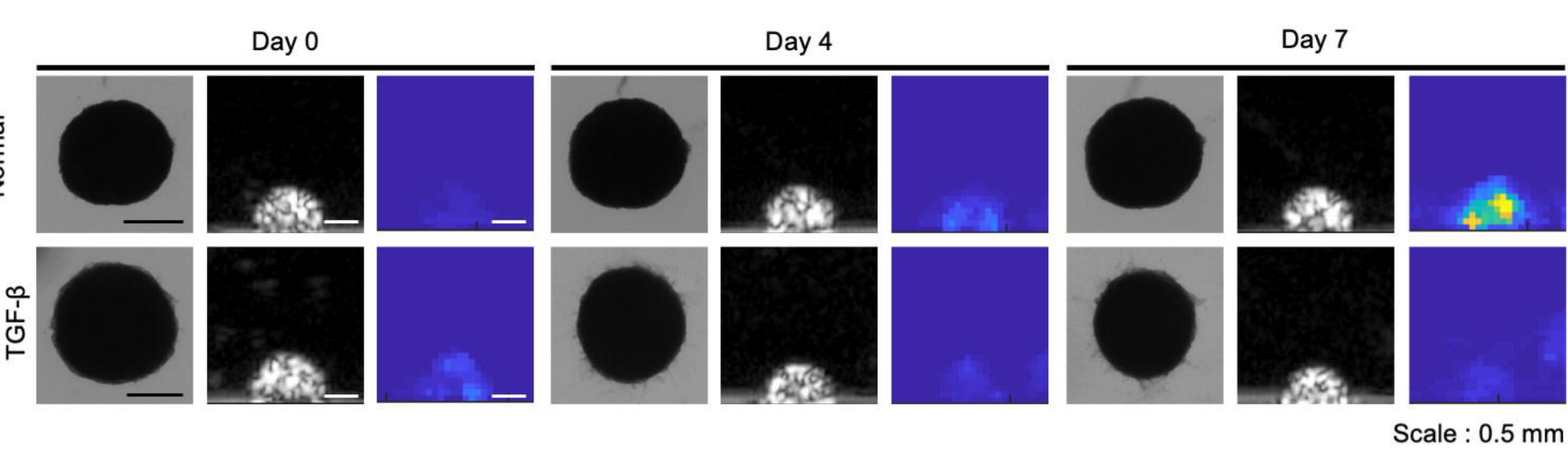
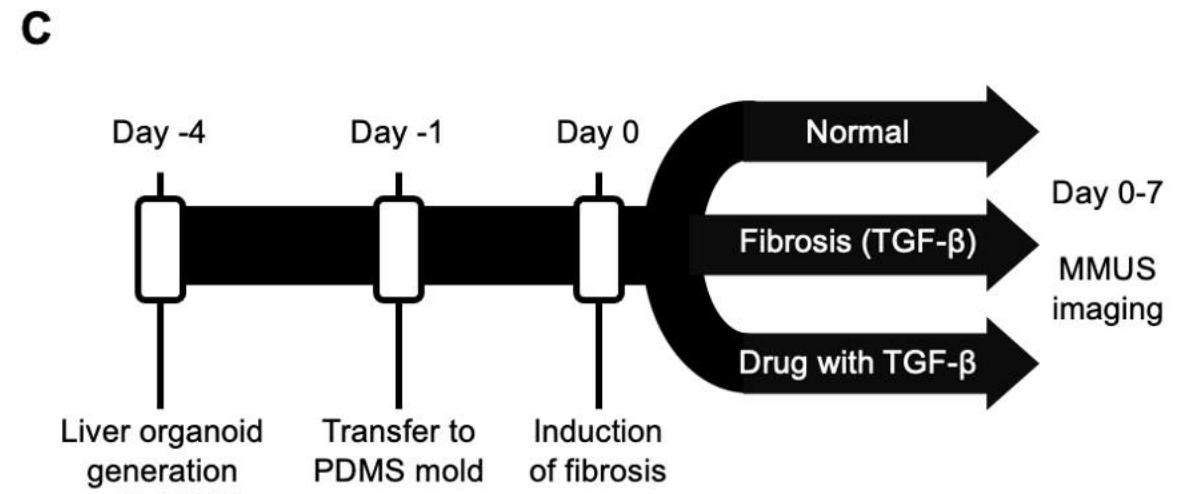
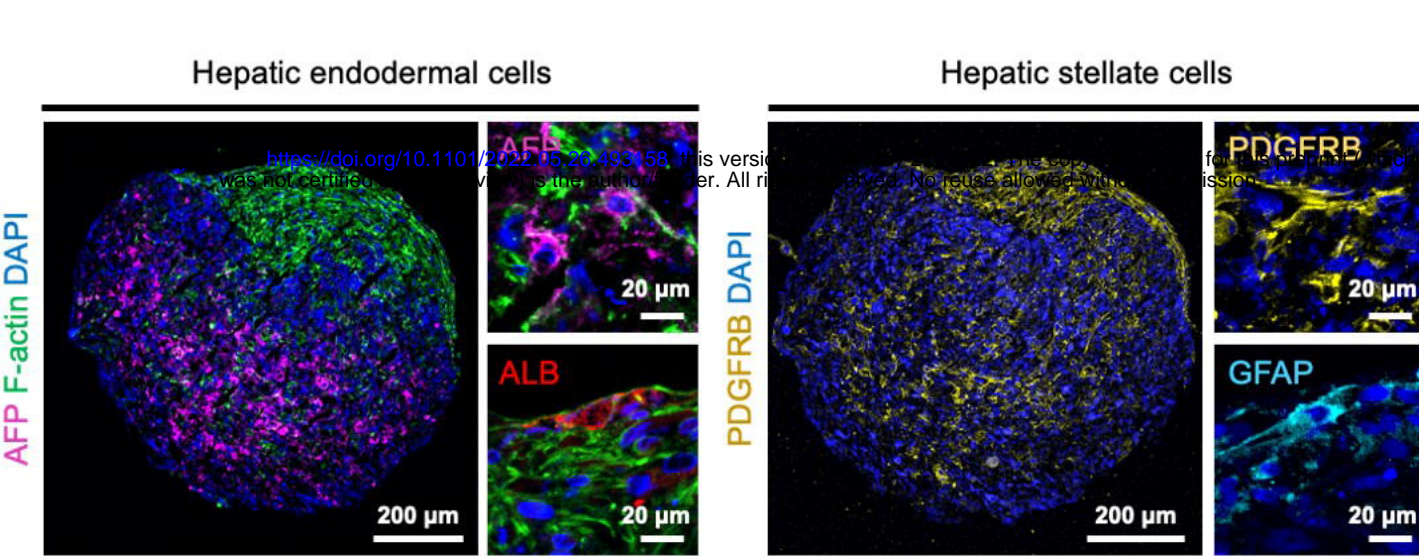
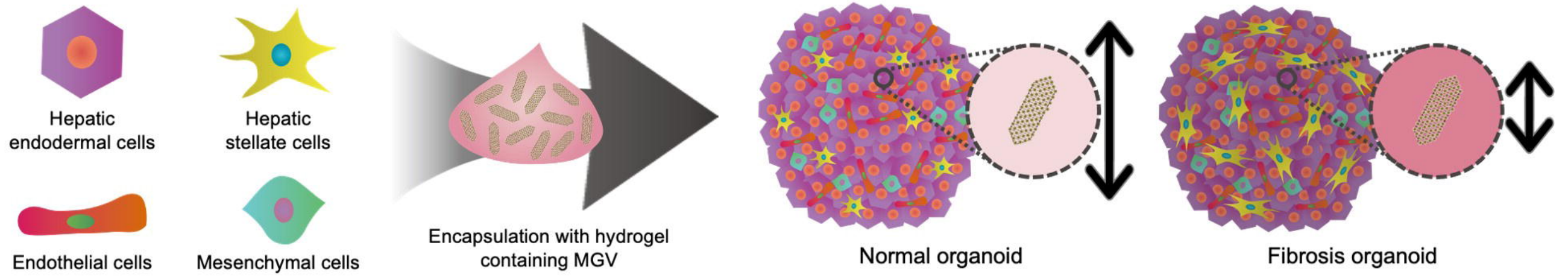
985 groups (scale bars = 200 μm in left images and 20 μm in right images). (e) Low-magnification
986 (left) and high-magnification (right) images of Sirius red-stained sections in two groups (scale
987 bars = 200 μm in left images and 20 μm in right images). (f) Quantification of the
988 hydroxyproline content in liver from two groups. For (b) Min and max in the parula and hot
989 color bars represent 0 and 500000, respectively, and the gray scale bar ranges from 0 to 1000000
990 arbitrary units. Error bars represent \pm SEM, and significance was determined using two-tailed
991 heteroscedastic *t*-tests with Welch's correction; *: $p < 0.05$; **: $p < 0.01$; ***: $p < 0.001$; ****:
992 $p < 0.0001$.
993

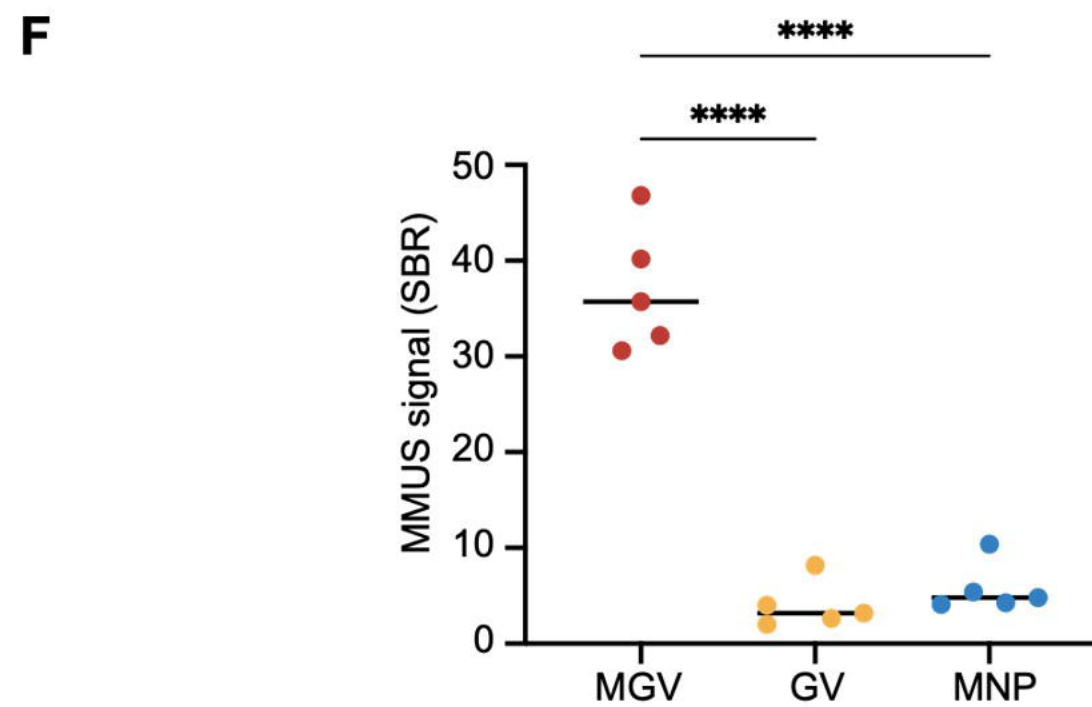
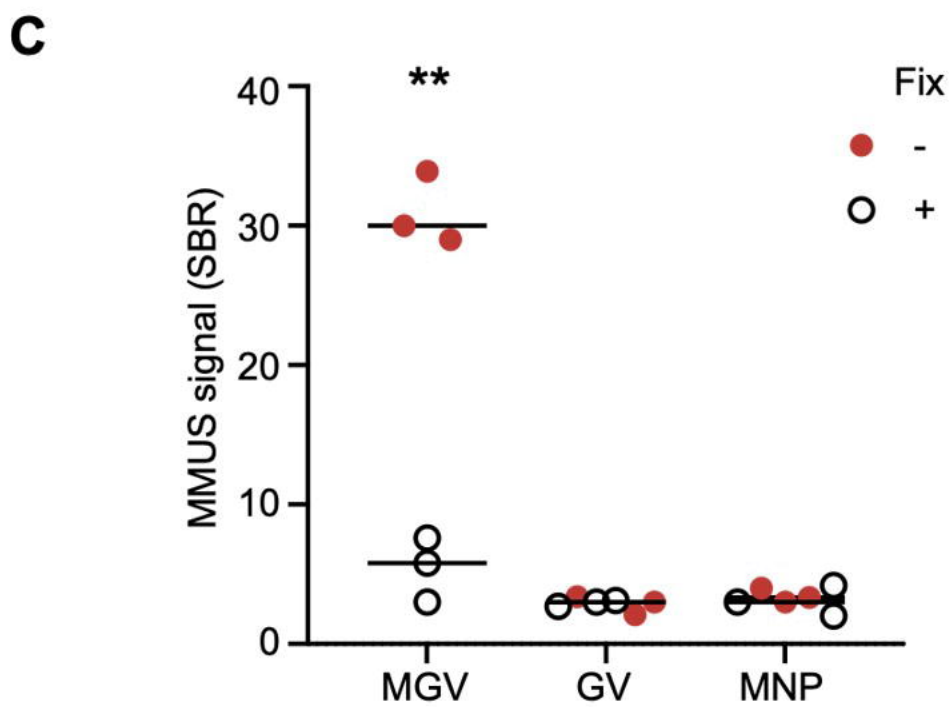
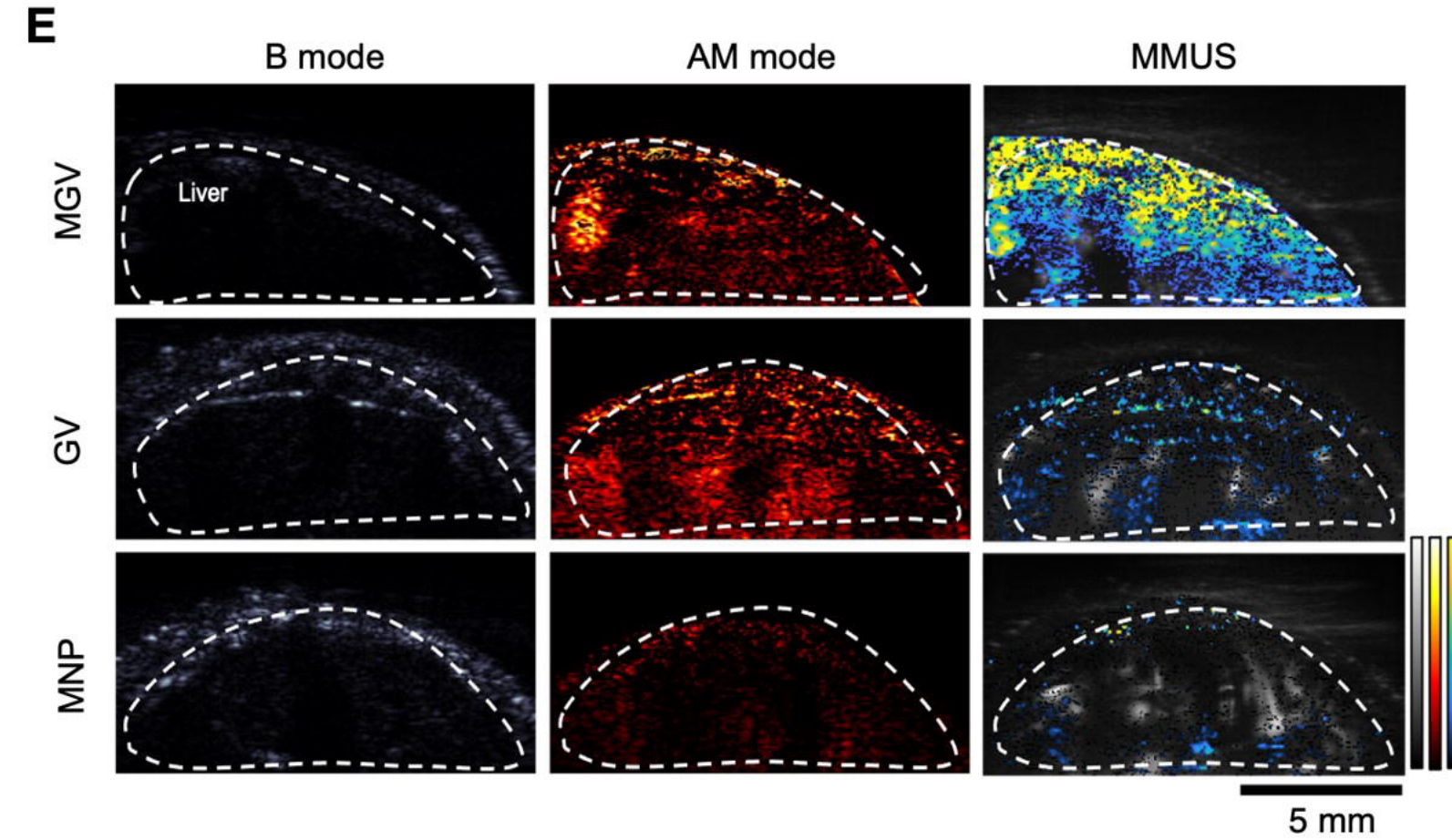
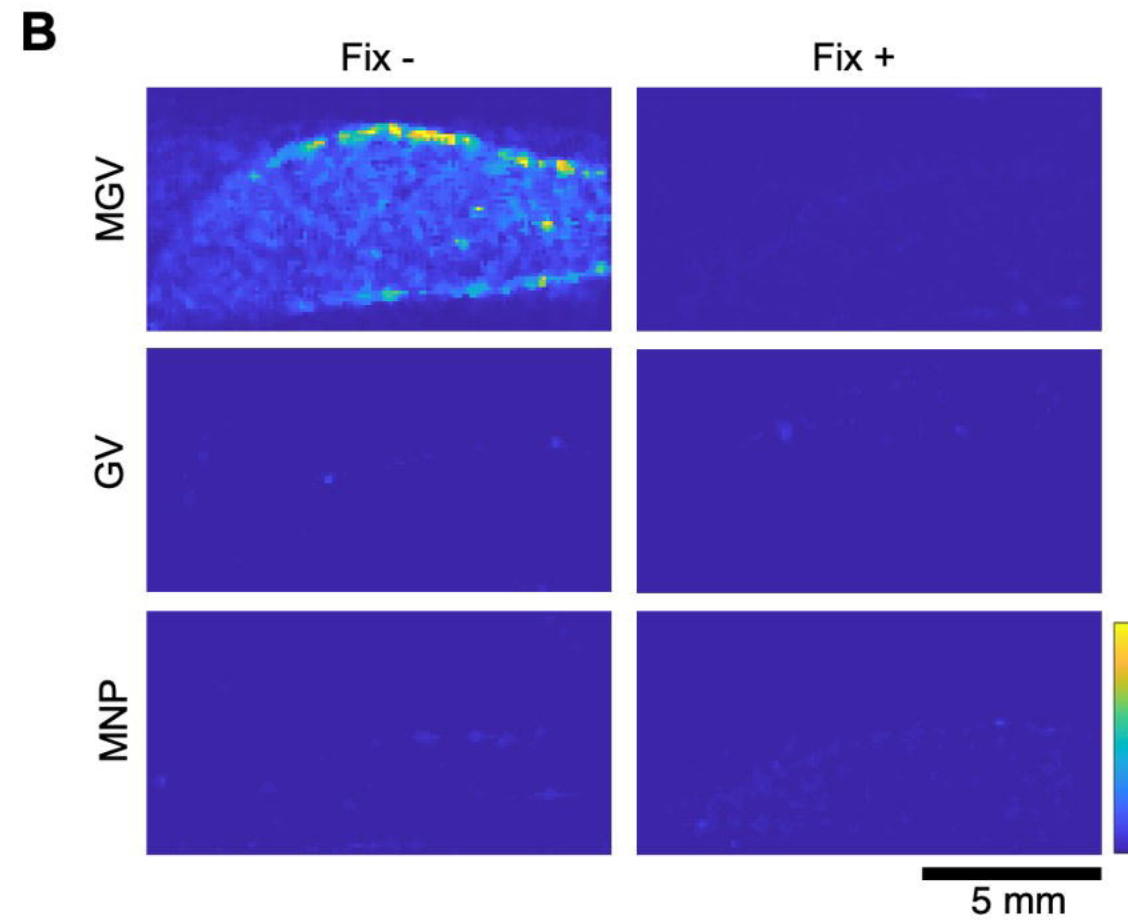
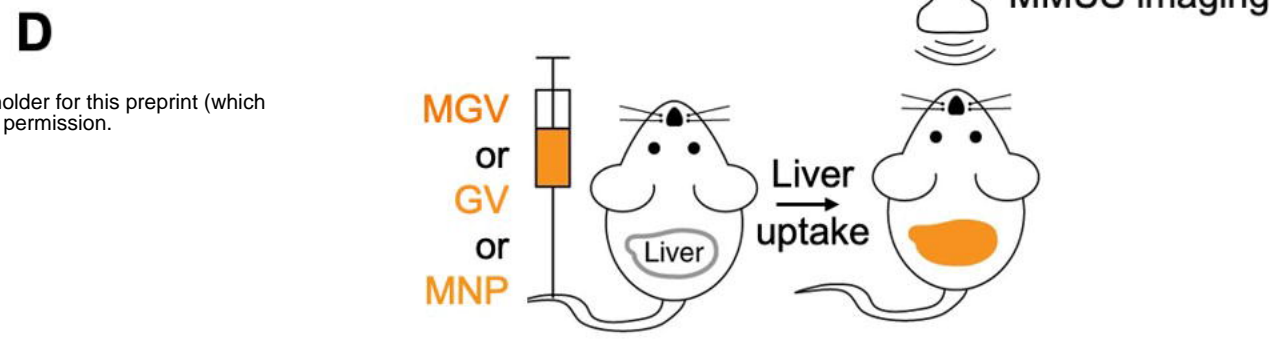
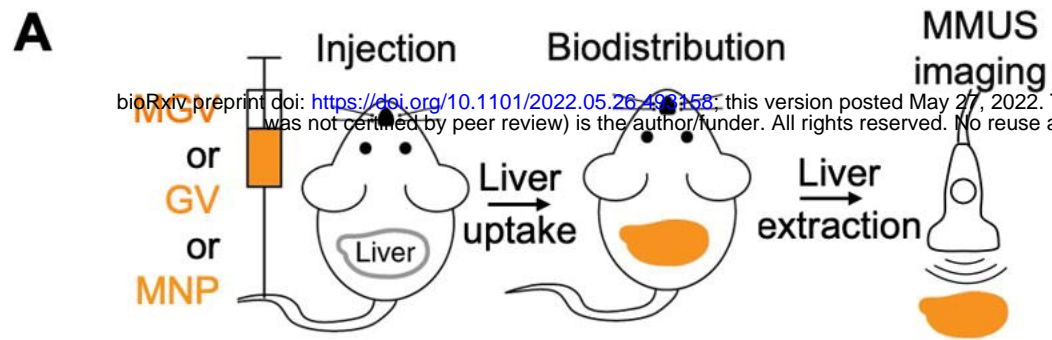


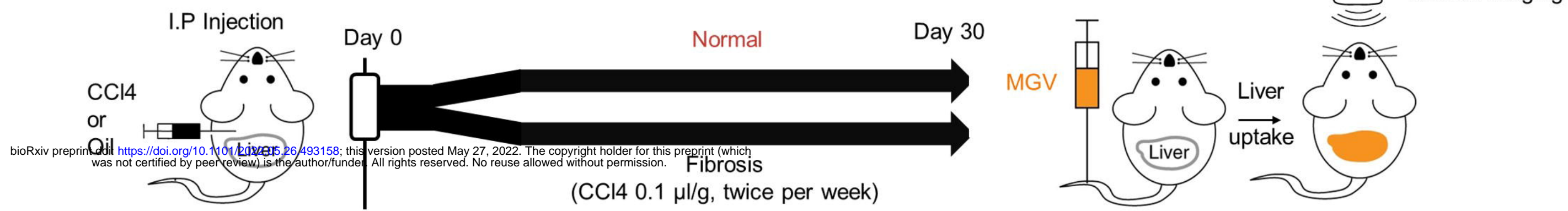




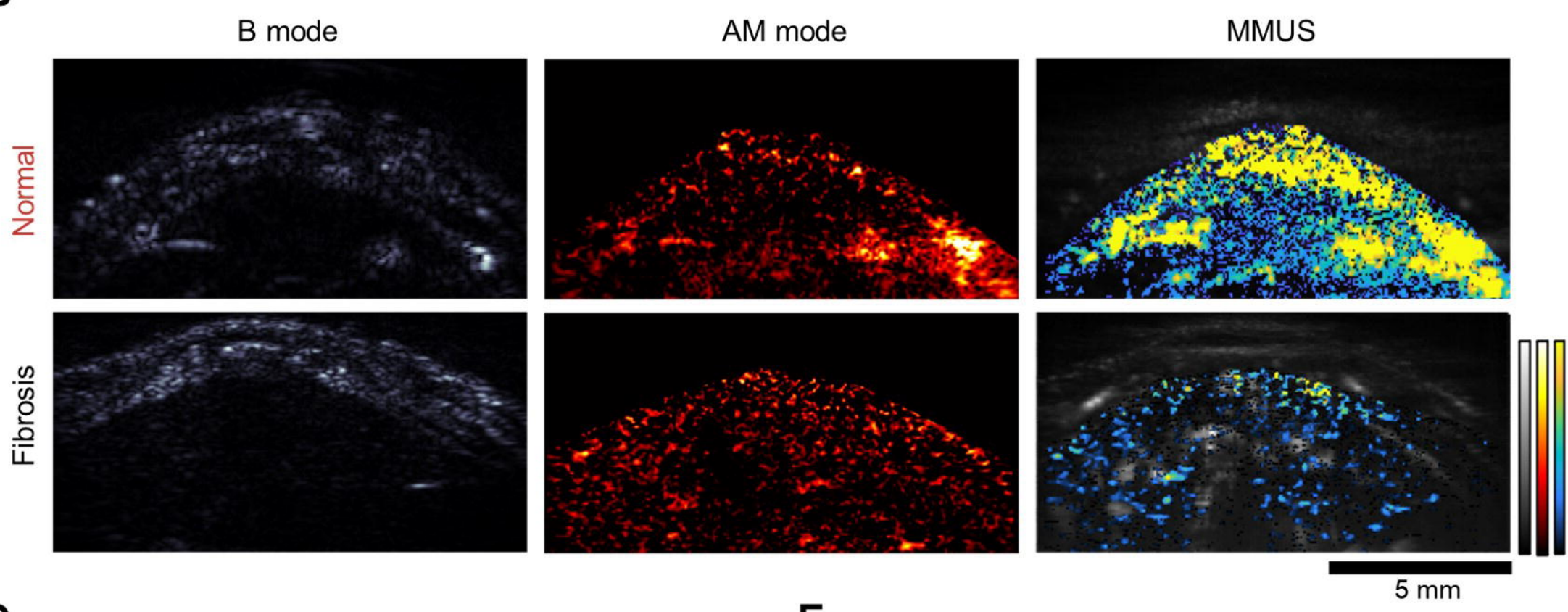
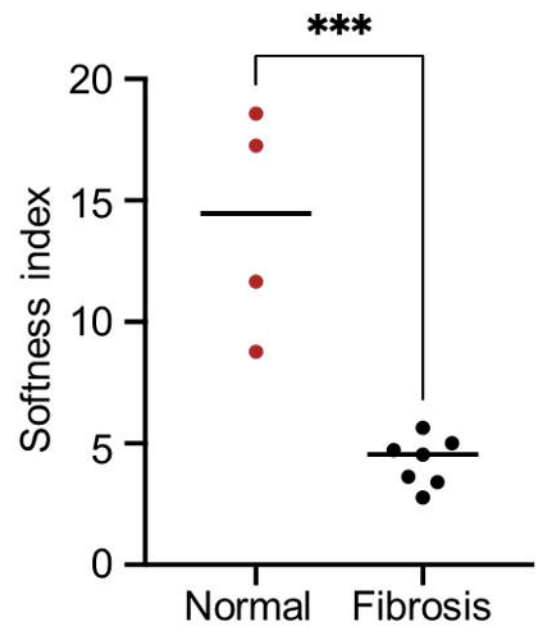
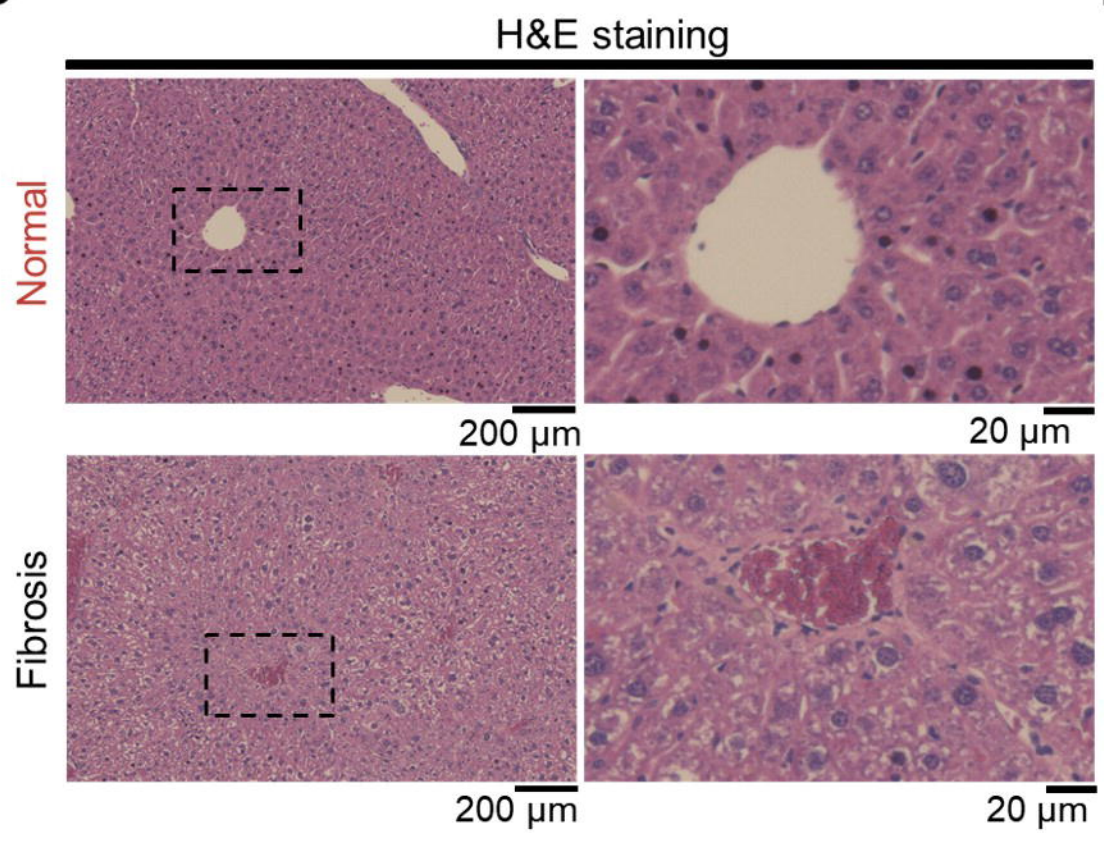
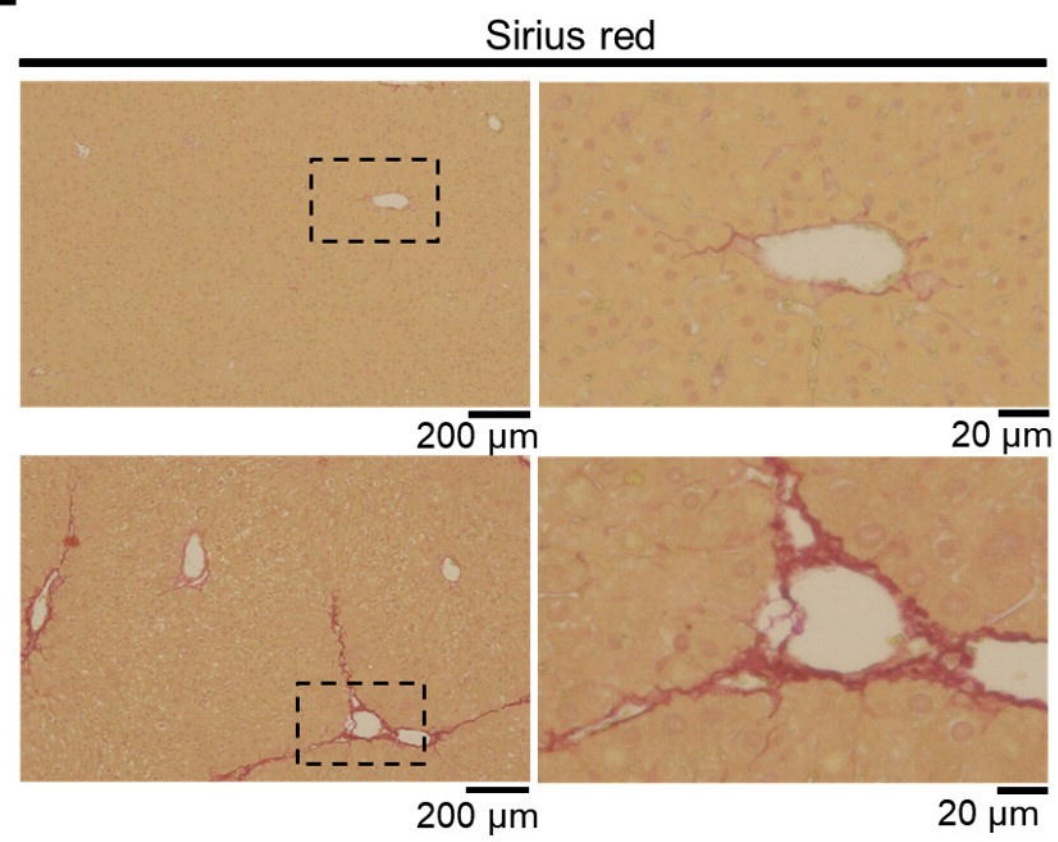
Liver organoid MGV incorporation model





A

bioRxiv preprint doi: <https://doi.org/10.1101/2022.05.26.493158>; this version posted May 27, 2022. The copyright holder for this preprint (which was not certified by peer review) is the author/funder. All rights reserved. No reuse allowed without permission.

B**C****D****E****F**